

Radiation-based analytic approaches to investigate the Earth's atmosphere

Thesis by
Tianhao Le

In Partial Fulfillment of the Requirements for the
Degree of
Doctor of Philosophy

The logo for the California Institute of Technology (Caltech), featuring the word "Caltech" in a bold, orange, sans-serif font.

CALIFORNIA INSTITUTE OF TECHNOLOGY
Pasadena, California

2022
Defended December 9, 2021

© 2022

Tianhao Le

ORCID: 0000-0002-6600-8270

All rights reserved except where otherwise noted

To my parents and love

ACKNOWLEDGEMENTS

It's sometimes hard to believe that my journey at Caltech has come to an end. The past five years and four months at Pasadena were certainly one of the most memorable times of my life. I appreciate the scientific training that I received here, and I have also enjoyed my time in Pasadena. Here I would like to take time to express my gratitude towards the people mentioned below who have been there with me through the ups and downs.

First of all, I would like to thank my advisor, Yuk Yung. This thesis would not have been possible without him. Yuk is a great mentor who has taught me valuable lessons both in science and in life. I thank Yuk for all the research advice that I am sure will benefit me in the long run. I am also grateful for his generosity for inviting me to all the dinners and parties, especially the ones at New Year that make me feel at home.

I would like to thank my other thesis committee members: Tapio Schneider, Paul Wennberg and Christian Frankenberg, for education and thoughtful considerations of my research. Tapio taught me about how to think about and discover scientific questions. Paul provided a lot of scientific guidance and support for my thesis. Christian gave me useful suggestions and encouragement for a new international graduate student. They have guided me towards the right direction.

I have also received great help from other professors in Caltech, special thanks go to Andy Ingersoll and John Seinfeld. Andy taught me how to understand a complicated thing using a simple model and also how to make a presentation. I also enjoyed and missed the Thanksgiving dinner I had with Andy's family. John provided me with excellent suggestions and help on my research. I also want to thank Andy Thompson, Jess Adkins, Simona Bordoni, Mike Brown, Dave Stevenson for their insightful classes and lectures. I sincerely owe my thanks to them.

Many colleagues from JPL and UCLA also significantly contributed to my research, particularly Yuan Wang, Vijay Natraj, Zhao-Cheng Zeng and Qing Yue. Yuan helped me to expand my view from the field I focused on to another. Thanks to Vijay for teaching me about radiative transfer modeling with great patience. Zhao taught me about the CLARS instrument and aerosol retrieval. I also benefited from Qing's knowledge on satellite products and clouds.

I would also like to thank current and past members in Yuk's group, who have been

a great source of help and support. I thank Run-Lie Shia for his advice and help on difficult problems in my research. It was my privilege to work with Yuk Army, Stuart Bartlett, Chao Liu, Qiong Zhang, Peter Gao, Pushkar Kopparla, Michael L. Wong, Siteng Fan, Jiazheng Li, Yangcheng Luo, Danica J. Adams, Sihe Chen and Jiani Yang.

I want to thank our administrative staff in GPS for their help in my study, including Margaret Carlos, Ulrika Terrones, Julie Lee, Irma Black, and Nora Oshima, for helping me with administration issues. I could not have focused on my research as I did without their support. I also want to thank Scott Dungan and Jian Ou for their help on server related issues. My thanks also go to Laura Flower Kim at ISP and Tess Legaspi at REGIS for their supports to international students.

It would not be possible to have a joyful graduate school experience without friends. I want to thank Wen Chen, Jun Chen, Zhaoyi Shen, Zhihong Tan, Yuanlong Huang and Lu Pan. They make my life in Caltech more enjoyable. I would like to thank the ESE graduate students who joined Caltech the same year as me: Liyin He, Siraput Jongaramrungruang, Harrison Parker, Katrina L. Hui and Kevin Vu. Thank you for preparing for the GPS social hour and Zilchbrau party together. I am also grateful for my brilliant office mates, including Ellen Leask, Yayaati Chachan and Maria Camarca. I had a good time talking with them.

Special thanks should be expressed to Xi Zhang and Cheng Li. They are more like mentors for me. They've always provided valuable guidance and warm encouragement throughout my life in Caltech. I enjoy all conversations with them about radiative transfer, clouds, dynamics, models, hikings and travel.

I would like to thank my dear friend, Jiaxin Qiao, for the great time in high school and Peking University, though we are thousands of miles away. I would also like to thank my undergraduate advisor, Yongyun Hu, who led me to the door of atmospheric science and put forward a lot of valuable comments on my research.

Finally, I would like to devote my thesis to my parents and my girlfriend. My parents, Maorong Le and Huidi Zhang, have not only given me life, but also offered me unconditional love and support. I would never have come this far without their love, trust and support. Last, but not least, I want to thank my girlfriend, Yanting Han. I am extremely lucky to have met Yanting during our time at Caltech. In Science, she helped me to proofread all my manuscripts and presentations. She also provided delicious meals in daily life. I feel honored to have her with me when I

moved to this new country, and her love let me grow up and learn how to love.

ABSTRACT

Radiation, propagating through Earth's atmosphere, plays an important role in the Earth system. Solar radiation is the major source of energy, followed by thermal infrared radiation emitted by the Earth. The total radiative energy budget affects dynamic, thermodynamics, photochemical and biological processes. In addition, by measuring the reflected and emitted radiation at a distance (e.g., satellite or aircraft), we can detect and monitor the physical characteristics of a region which can help researchers get a better understanding of Earth's atmosphere. Therefore, radiation-based analytic approaches are powerful tools in Earth Science. This thesis focuses on using radiation-based analytic tools to study the Earth's atmosphere and to understand human impacts on the Earth system.

First, we develop novel machine learning methods for hyperspectral radiative transfer simulations. Hyperspectral technique is one of the most popular and powerful methods for atmospheric remote sensing and is widely used for temperature, gas, aerosol, and cloud retrievals. However, accurate forward radiative transfer simulations are computationally expensive since they require a larger number of monochromatic radiative transfer calculations. We, therefore explore the feasibility of machine learning techniques for fast hyperspectral radiative transfer simulations that perform calculations at a small fraction of hyperspectral wavelengths and extend them across the entire spectral range. The machine learning-based approach achieves better performance than the traditional principal component analysis (PCA) method.

Second, we evaluate modeled hyperspectral infrared spectra against satellite all-sky observations. The national weather centers obtain data from hyperspectral infrared sounders on a global scale. The cloudless scenario of this data is used to initialize weather forecasts, including temperature, water vapor, water cloud, and ice cloud profiles on a global grid. Although the data from these satellites are sensitive to the vertical distribution of ice and liquid water in the clouds, this information is not fully utilized. In this study, we evaluate how well the modeled spectra compare to AIRS observations using different cloud overlap models. We hope that this information can be used to verify clouds in the National Meteorological Center model and to initialize forecasts in the future .

In the last chapter, we use radiation-based analytic approaches to study human impacts on the Earth system. In the first study case, we show that the radiative

forcing due to geospatially redistributed anthropogenic aerosols mainly determined the spatial variations of winter extreme weather in the Northern Hemisphere during 1970-2005, which is a unique transition period for global aerosol forcing. In the second case, we review satellite and ground-based observations and conduct state-of-art atmospheric model simulations during the COVID-19 lockdown period. The halted human activities during the COVID-19 pandemic in China provided a unique experiment to assess the efficiency of air-pollution mitigation.

PUBLISHED CONTENT AND CONTRIBUTIONS

- [1] T. Le, C. Liu, B. Yao, V. Natraj, and Y. L. Yung. “Application of machine learning to hyperspectral radiative transfer simulations”. In: *Journal of Quantitative Spectroscopy and Radiative Transfer* 246 (2020), p. 106928. doi: 10.1016/j.jqsrt.2020.106928.
T.L. participated in the conception of the project, designed and analyzed the models, prepared the data, and participated in the writing of the manuscript.
- [2] T. Le, Y. Wang, L. Liu, J. Yang, Y. L. Yung, G. Li, and J. H. Seinfeld. “Unexpected air pollution with marked emission reductions during the COVID-19 outbreak in China”. In: *Science* 369.6504 (2020), pp. 702–706. doi: 10.1126/science.abb7431.
T.L. participated in the conception of the project, prepared and analyzed the data, and participated in the writing of the manuscript.
- [3] Y. Wang, T. Le, G. Chen, Y. L. Yung, H. Su, J. H. Seinfeld, and J. H. Jiang. “Reduced European aerosol emissions suppress winter extremes over northern Eurasia”. In: *Nature Climate Change* 10.3 (2020), pp. 225–230. doi: 10.1038/s41558-020-0693-4.
T.L. performed the LWA calculations, analyzed the simulations data, and participated in the writing of the manuscript.

4.2.5	Appendix	46
4.2.5.1	Recipe for the calculation of local wave activity	46
4.3	Unexpected air pollution with marked emission reductions during the COVID-19 outbreak in China	48
4.3.1	Introduction	48
4.3.2	Methods and data	48
4.3.2.1	Satellite product	48
4.3.2.2	Ground station observations	49
4.3.2.3	Reanalysis data	49
4.3.2.4	WRF-Chem model simulations	50
4.3.3	Results	52
4.3.4	Conclusion	60
	Bibliography	62

LIST OF ILLUSTRATIONS

<i>Number</i>	<i>Page</i>
1.1 Earth's energy budget(Credit:NASA)	2
2.1 Schematics of the Neural-network (NN) based and principal component analysis (PCA) based models for fast hyperspectral radiative transfer simulations.	8
2.2 (a) Training and (b) validation losses of the four different optimization algorithms for simulations of the OCO-2 O ₂ -A band radiances.	13
2.3 (a) Sample OCO-2 O ₂ A-band observation; (b) Accuracy of PCA-based and NN-based HRT simulations using 50 channel radiances as inputs. The normalized photon number is defined as the ratio of the photon number to its maximum value over the entire spectral range.	14
2.4 Same as Fig.2.3 but for the two CO ₂ absorption bands measured by OCO-2.	15
2.5 Mean absolute relative errors given by the PCA-based and NN-based fast HRT models as a function of the number of input channel radiances. The results are ensemble averaged over 20,000 tests.	16
2.6 Same as Fig. 2.3 but for monochromatic RT simulations over the solar spectral range from 0.75–0.92 μm	17
2.7 Cumulative probability distributions of (a) spectrally averaged mean absolute REs, (b) maximum REs and (c) mean largest-500 REs for 2,000 atmospheric scenarios.	17
3.1 Two probability distributions that have a Pearson correlation coefficient of 1.0 and yet are clearly very different.	24
3.2 Probability distributions of the difference between surface temperature and brightness temperature at three atmospheric window channels. (901 cm^{-1} , 1231 cm^{-1} and 2615 cm^{-1}) for the non-frozen ocean day and night scenarios. The AIRS observations, CRTM with average overlap scheme, maximum-random overlap scheme, random overlap scheme, and maximum overlap scheme results are shown in dashed black, red, blue, green, and orange lines, respectively.	27
3.3 Same as Figure 2, but for tropical zone only.	29
3.4 Same as Figure 2, but for mid-latitude zone only.	30

3.5	Same as Figure 2, but for polar zone only.	31
3.6	(a) Mean brightness temperature, (b) mean absolute difference of brightness temperature, and (c) the first Wasserstein distance between CRTM radiance simulations and all 82,271 AIRS observations for 846 selected AIRS channels between 790 cm^{-1} to 1231 cm^{-1} . The AIRS observations, CRTM with average overlap scheme, maximum-random overlap scheme, random overlap scheme, and maximum overlap scheme results are shown in dashed black, red, blue, green, and orange lines, respectively.	32
3.7	Visualization of all 82,271 cases on a global map of 901 cm^{-1} for (a) AIRS observations, (b) CRTM with average overlap scheme, and (c) difference between AIRS observations and CRTM-avg.	33
4.1	CLWA trends from reanalysis and model simulation over December to February during 1970–2005. a–e, Spatial patterns of LWA trends (left column) and their zonal mean distribution (right column) for: JRA55 (a); JRA55 with removal of trends in major known climate oscillation indices (b); CESM ALL results (c); CESM NO_AERO results (d); and CESM ALL – NO_AERO (DIFF) (e). Black dots (each representing 16 grid points) indicate that the local linear trend is significant at the 90 % confidence level using a Student’s t-test. Shading in the zonal mean plots indicates spread of the LWA trend at the same latitude. The red vertical bars denote latitude zones with significant LWA trends (shades do not overlap with the 0 m^2 per decade line).	41
4.2	Climatology and trends (1970-2005) of cyclonic and anticyclonic wave activities based on JRA-55.	42
4.3	Northern Hemispheric trends of jet stream sinuosity and local wave activity (LWA) during 1970-2005 based on JRA55 Reanalysis. The bottom panel shows the results with removal of natural variability (NAT) by the multivariate linear regression method.	43
4.4	Same with Figure 1 but for top 10% LWA during each season. They indicate the extreme LWA cases and strongest cyclonic/anticyclonic events.	43
4.5	Comparison of climatological geopotential height at 500 hPa (Z500) and local wave activity (LWA) between JRA-55 and the CESM all forcing experiment.	44

- 4.6 (a) Z500 as a function of longitude and latitude. (b) The eddy term \hat{z} plotted between the latitude 50N and the contour with the equivalent latitude $\phi_e = 50N$. (c) LWA at 50N as a function of longitude (red). The product of the zonal amplitude \hat{z} and meridional amplitude $\hat{\phi}$ of a planetary wave (blue). In the small amplitude limit, $LWA = -0.5a\hat{z}\hat{\phi}$ (d) -LWA as a function of longitude and latitude. In (a), (b) and (d), the contour with the equivalent latitude $\phi_e = 50N$ shown in solid red, and the latitude 50N is in dashed red. 47
- 4.7 Accumulated fire counts based on MODIS Active Fire Products over three-week periods during 2020-CLD and 2019-CLIM. Fire counts can be used to indicate the biomass burning in the agricultural activities. Dots in the plots are with confidence level larger than 80 in the MODIS product. 50
- 4.8 Spaceborne measurements of NO₂ from TROPOMI. (A) Column-integrated NO₂ averaged over the COVID19 lockdown period (CLD) for three weeks during Jan. 23 to Feb. 13, 2020. (B) Column-integrated NO₂ averaged over the reference period in 2019. To account for the annual holiday, the 2019 reference period we choose is the same as that in 2020-CLD in the Chinese lunar calendar, starting from the two days before the Chinese Lunar New Year (2019-LNY). Note that TROPOMI NO₂ is available only starting from June 2018. (C) The fractional changes between (A) and (B), calculated only for the regions with NO₂ in 2019-LNY greater than 0.2 DU. The symbols in the maps indicate the location of Wuhan, the most affected city by the COVID-19 disease. 1 Dobson Unit (DU) = 0.4462 mmol m⁻². . . 53

4.9 Ground-based station observation of particulate matter (aerodynamic diameter less than $2.5 \mu m$, PM2.5), NO₂, SO₂, and ozone in eastern China including four megacities (A. Wuhan, B. Beijing, C. Guangzhou, and D. Shanghai). The figure compares the three-week averages during the city lockdown period (CLD), the three-week averages before the city lockdown (pre-CLD), the five-year climatology for 2015-2019 during the same period with CLD in the Chinese lunar calendar that covers the Lunar New Year (CLIM-LNY), and the five-year climatology for 2015-2019 during the same period with CLD in the Gregorian calendar (CLIM). Error bars indicate the standard deviations over multiple years. (E) The map of surface PM2.5 changes in 2020-CLD compared to CLIM-LNY based on the 1515 state monitoring stations. The low-resolution patterns in the north and west are caused by the sparsity of stations. Two boxes indicate the Beijing-Tianjin-Hebei and central China regions. For ozone, $1 \mu g m^{-3}$ is approximately about 0.47 ppb under a standard condition. . 55

4.10 Daytime variation of ozone and NO₂ (10:00 to 16:00 LST) as a function of PM2.5 in the winter from 2015 to 2019 (A) and during 2020-CLD (B). During wintertime in north China, the weak insolation slows the atmospheric photochemistry processes. Therefore, very high NO_x emissions in the region cause remarkable ozone titration even during daytime, as shown in A, particularly with increasing PM2.5 which further attenuates the incoming solar radiation. However, during 2020-CLD, significant decrease in NO_x emissions alleviates the ozone titration, and during haze episodes, the ozone level is much higher than that during the winter from 2015 to 2019. The ozone concentration fluctuates at around $65 \mu g m^{-3}$ with PM2.5 exceeding $35 \mu g m^{-3}$, caused by complicated nonlinear ozone chemistry. 56

4.11 MODIS L3 AOD from Terra and Aqua during the same three-week period with 2020-CLD from 2015 to 2020. 56

4.12	Fractional changes (%) in meteorological conditions between the 2020-CLD and the lunar new year climatology (CLIM-LNY) during 2015-2019 based on the ERA5 reanalysis data. (A) 1000-hPa relative humidity, (B) 10-meter wind speed (contours) and wind direction (vectors), (C) boundary-layer height, and (D) daily precipitation. Symbols in the maps indicate the location of the four major cities in Figure 4.9.	57
4.13	WRF-Chem simulated aerosol species and precursor gases during the COVID-19 city lockdown period in the Beijing-Tianjin-Hebei region, and their sensitivity to the altered emissions, meteorological conditions, and chemical pathways. (A) Time evolution of surface PM _{2.5} concentrations in the ground-based observations (black dots), the baseline simulation (blue line), and the sensitivity simulation with the climatological (2015-2019) meteorological conditions (red line, see details in Table 4.2). (B) The same with (A) but for ozone. (C) The simulated fractional changes in different aerosol species in response to changes in NO _x emissions, meteorological conditions, and the representation of heterogeneous chemistry. (D) The same with (C) but for gaseous pollutants including NO ₂ , SO ₂ , and O ₃	58
4.14	WRF-Chem simulated surface aerosol species over two characteristic regions: Beijing-Tianjin-Hebei in northern China and Central China. OA and EC are short for organic aerosol and elementary carbon, respectively.	59
4.15	Simulated sensitivity of aerosol species and precursor gases to the VOC changes by 30%.	60

LIST OF TABLES

<i>Number</i>	<i>Page</i>
2.1 Parameters of the NN-based model for the four cases considered in this study, including the number of scenarios used for training and validation, total number of channels, and dimensions of the hidden layers. The MAE and ReLu are used as the loss and activation function, respectively, and Adaptive Moment Estimation (AdaM) is used as the optimizer.	12
3.1 Summary of all 82,271 non-frozen oceans AIRS observations from 2018/10/31 21:00 UTC to 2018/11/01 21:00 UTC. We denote $ \text{lat} \leq 30$, $ \text{lat} \in (30,60]$, and $ \text{lat} > 60$ are tropical zone, mid-latitude zone, and polar zone, respectively.	25
3.2 Comparison of performance of CRTM with average overlap, maximum-random overlap, random overlap, and maximum overlap scheme for non-frozen ocean all (day and night), day only, night only scenarios using the first Wasserstein distance. The best performance models for each column are marked in red.	28
4.1 WRF-Chem model configurations.	51
4.2 Model sensitivity experiment description.	52

Chapter 1

INTRODUCTION

1.1 Background

Since the beginning of atmospheric science, the study of atmospheric radiation and radiative transfer has been of great importance since radiative transfer is a fundamental factor affecting the atmospheric circulation and climate of the planet. It's also widely used in many other areas, including planetary science, astrophysics, applied physics, optics, and engineering disciplines.

At the beginning of the 20th century, astrophysicists pioneered the field of radiative transfer research. Schuster (1905) first studied radiative transfer in foggy atmospheres [1], in which he considered the contribution of two separate beams, upward and downward, which was the origin of the two-stream approximation. In 1906, Schwarzschild substituted the two-beam solution in the integral equation to explain the limb darkening of the Sun and used this method to determine the continuous distribution of the radiation field [2]. In Schwarzschild (1914), he proposed that a medium can be both an absorber and an emitter in thermal equilibrium and used this as a basis for the Schwarzschild equation [3]. In 1916, Eddington first used the Legendre polynomial to treat the physical structure of the interior of a star and thus developed an intensity expansion, which formed the Eddington approximation in radiative transfer [4].

Before 1950, the subject of the radiative transfer problem was mainly studied by astrophysicists, although it was also an important field of research in nuclear and applied physics related to neutron migration. In Chandrasekhar's landmark book "Radiative Transfer", which was published in 1950, he pointed out that the problem of radiative transfer in plane-parallel atmospheres should be a branch of mathematical physics [5]. Since then, the radiative transfer problem has received attention from theoretical physicists.

The above papers and works laid a solid theoretical foundation for the basic principles of radiative transfer. In the 1960s, the rapid development of remote sensing by meteorological satellites and Mainframe computers significantly promoted theoretical and experimental research on atmospheric radiative transfer, which led to the flourishing of atmospheric radiative transfer science [6, 7]. Another important

reason for the development of atmospheric radiative transfer is that people pay more and more attention to global climate change and the impact of human activities on the future climate environment, and in these topics, radiative transfer plays an important role. Specifically, it is important for the planetary energy budget and remote sensing.

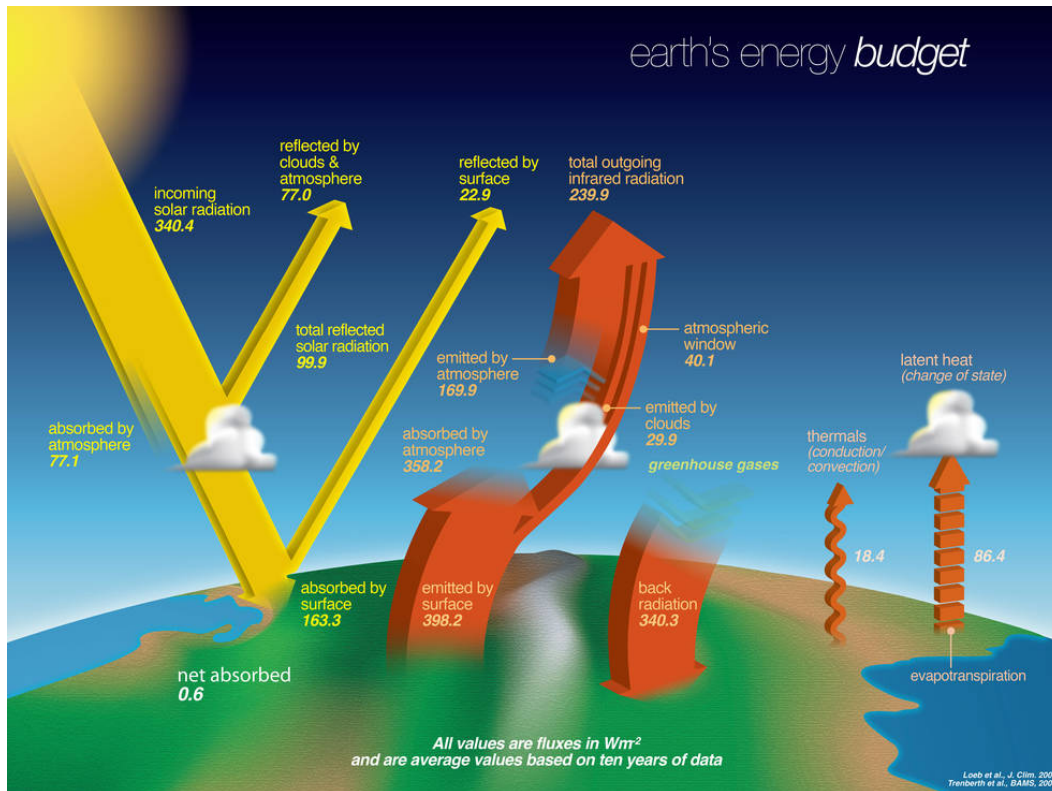


Figure 1.1: Earth's energy budget(Credit:NASA)

The Earth radiation budget accounts for the balance between the incoming solar radiation and outgoing thermal infrared radiation from the Earth (Figure 1.1). An unbalanced radiation budget will cause the temperature of the Earth's atmosphere to rise or fall, and ultimately affect our climate through dynamic, thermodynamics, photochemical and biological processes [8, 9]. To understand climate change, we must determine what drives the changes within the Earth radiation budget first.

High quality observations are the key to understanding the fundamental physical processes underlying radiative transfer through the atmosphere. Remote sensing techniques take advantage of wavelength-dependent absorption and scattering processes by gases and particles to retrieve the physical properties and chemical com-

positions of the atmosphere (e.g., temperature, moisture content, CO₂, O₃, CH₄, NO₂, aerosols), which serve as inputs to climate models.

1.2 Hyperspectral remote sensing and modeling

With an increasing need for detection and monitoring of land surface, atmosphere, ocean, and space targets, scientists are paying more and more attention to the research and development of instruments with both high spatial resolution and high spectral resolution. Hyperspectral remote sensing is a technique of continuous remote sensing imaging of ground objects with very narrow and continuous spectral channels, which is developed on the basis of imaging and spectroscopy. It has the unique advantages of high spectral resolution, which is a revolutionary leap in the development history of remote sensing technology. Unlike ground-based spectroradiometer, hyperspectral remote sensing acquires not spectral measurements on points, but spectral measurements on continuous space so that it can obtain image information and spectral information of the target at the same time. Compared with traditional remote sensing, hyperspectral remote sensing provides very narrow imaging bands for each imaging image element, with resolution is up to the order of nanometers, and the number of spectral channels is up to tens or even hundreds. As a result, it obtains more spectral information, which can provide a wider range of applications in earth observation and environmental investigation. Instruments using hyperspectral technique include the the Atmospheric Infrared Sounder (AIRS) onboard the Aqua satellite, the Cross-Track Infrared Sounder (CrIS) onboard the Suomi-NPP satellite, the Orbiting Carbon Observatory-2 (OCO-2), the Ozone Monitoring Instrument (OMI), and its successor, the TROPOspheric Monitoring Instrument (TROPOMI).

A large number of satellite and ground-based hyperspectral measurements require forward radiation transfer models for instrument calibration and retrieval applications. Due to the significant spectral variation of molecular absorption, hyperspectral radiative transfer model has to be performed at a fine spectral resolution that is typically significantly better than the instrument resolution. The rigorous approach is to use line-by-line RT calculations; however, this requires a large number of computationally expensive simulations, making it impractical for satellite applications. As a result, significant effort has been devoted to the development of fast hyperspectral radiative transfer models. Previous studies found that by using a Principal Component Analysis based method, they can achieve a speedup of more than 50 times compared to the line-by-line monochromatic simulations [10, 11, 12, 13, 14]. However, this

method relies on a linear procedure for the extension, which lacks theoretical basis given the highly nonlinear variation of gas absorption with wavelength. Therefore, a nonlinear regression method is needed.

1.3 Outline of this thesis

This thesis work is composed of three parts. In Chapter 2, A neural network model is used as an example for the development of the fast hyperspectral radiative transfer, and its results are compared with those from a principal component analysis model. In Chapter 3, we evaluate modeled hyperspectral infrared spectra against satellite all-sky AIRS observations using different cloud overlap assumptions. We also present two example cases to study the human impacts on the Earth system by using radiation-based analytic tools in Chapter 4. More specifically, one studies the radiative forcing due to geo-spatially redistributed aerosols, and the other uses hyperspectral satellite retrieved NO₂ and model simulations to understand haze formation.

APPLICATION OF MACHINE LEARNING TO HYPERSENSPECTRAL RADIATIVE TRANSFER SIMULATIONS

- [1] T. Le, C. Liu, B. Yao, V. Natraj, and Y. L. Yung. “Application of machine learning to hyperspectral radiative transfer simulations”. In: *Journal of Quantitative Spectroscopy and Radiative Transfer* 246 (2020), p. 106928. DOI: [10.1016/j.jqsrt.2020.106928](https://doi.org/10.1016/j.jqsrt.2020.106928).

2.1 Introduction

Spectral variation of radiance provides rich information for remote sensing of atmospheric temperature, gas, aerosol, and cloud [15, 16]; hyperspectral radiative instruments have, therefore, become essential tools for atmospheric monitoring and measurements [17, 18]. Instruments employed for atmospheric profile retrieval include the Atmospheric Infrared Sounder (AIRS) onboard the Aqua satellite, which has 2378 channels covering the spectral region from 3.7 to 15.4 μm [19], and the Cross-Track Infrared Sounder (CrIS) on-board the Suomi-NPP satellite, which measures radiance spectra in 1305 channels between 3.92 and 15.38 μm [20, 21]. The Infrared Atmospheric Sounding Interferometer (IASI) has even higher spectral resolution with 8461 channels covering wavelengths from 3.62 to 15.5 μm [22]. A hyperspectral sounder, the Geostationary Interferometric Infrared Sounder (GIIRS), is on the Chinese Fengyun-4A geostationary satellite [23]. Instruments with higher spectral resolutions are frequently utilized for atmospheric trace gas retrievals. The Ozone Monitoring Instrument (OMI) has 740 spectral channels ranging from 0.27 to 0.5 μm [24], and its successor, the TROPOspheric Monitoring Instrument (TROPOMI), measures key atmospheric constituents in over 900 channels from 0.27 up to 2.385 μm [25]. The Ozone Mapping and Profiler Suite (OMPS) on board Suomi-NPP and the NOAA-20 (JPSS1) operational satellite cover the wavelength ranges from 250–310 nm (Nadir Profiler) and 300–380 nm (Nadir Mapper) with a spectral resolution less than 1.1 nm [26]. The Global Ozone Monitoring Experiment-2 (GOME-2) on METOP-A and METOP-B senses the Earth’s backscattered radiance and extraterrestrial solar irradiance from 240–790 nm with 4096 spectral channels [27]. Satellites monitoring CO_2 , such as the Orbiting Carbon Observatory-2 (OCO-2) and TanSat, include 3000 channels covering the oxygen

A-band and strong and weak CO₂ absorption bands from 0.76 to 2.08 μm [28, 29]. Meanwhile, some ground-based hyperspectral instruments have also been developed, such as the Total Carbon Column Observing Network [30] and the California Laboratory for Atmospheric Remote Sensing [31, 32]; the latter covers the spectral range between 0.66 and 2.5 μm with a resolution of 0.06 cm^{-1} .

The large number of satellite- and ground-based hyperspectral measurements necessitates forward radiative transfer (RT) models for instrumental calibration and retrieval applications. Due to the significant spectral variation of molecular absorption, hyperspectral RT (HRT) has to be performed at a fine spectral resolution that is typically significantly better than the instrument resolution. The rigorous approach is to use line-by-line (LBL) RT calculations; however, this requires a large number of computationally expensive simulations, making it impractical for satellite applications. As a result, significant effort has been devoted to the development of fast HRT models.

By separating the single and multiple scattering contributions and treating multiple scattering with a double- k approach, Duan et al. developed a fast RT model for simulating the oxygen A-band spectrum [33]. Zhang et al. used pre-computed lookup tables (LUTs) of bidirectional reflectance/transmission distribution functions and effective emissivity of scattering layers to alleviate the computational burden for multiple scattering [34]. Wang et al. used LUTs for clear layer effective temperature as well; their improved LUT-based model is four to five orders of magnitude faster than a 32-stream discrete ordinates RT model in the infrared spectral region [35]. Natraj et al. found that the differences between approximated radiances efficiently given by a combination of two-stream and single-scattering simulations and those from numerically exact simulations can be quantified using principal component analysis (PCA) [10]. The PCA model achieved a speedup of more than 50 times compared to monochromatic simulations, and has been significantly improved since then [10, 11, 12, 13, 36, 37].

The aforementioned models improve the computational efficiency by accelerating every single RT simulation. A different category of fast HRT models performs a reduced number of RT simulations, and extends the resulting radiances at a limited fraction of wavelengths to the complete hyperspectral wavelength grid. Since little computational time is required for the extension procedure, significant improvement in computational efficiency is achieved. Examples of this approach include the PCRTM model [38, 16] and the optimal spectral sampling (OSS) method [39].

The essential difference between the PCRTM and OSS models is in how radiances at the carefully chosen monochromatic wavelengths are used to obtain the full channel radiances. PCRTM calculates the principal components (PC) of the full spectral radiances for a large number of different atmospheric scenarios, and uses PC scores predicted from the limited set of monochromatic radiances for the extension. The OSS approach directly generates weighting factors for each monochromatic wavelength and corresponding channels. It should be noted that both PCRTM and OSS rely on a linear procedure for the extension, which lacks theoretical basis given the highly nonlinear variation of gas absorption with wavelength.

Machine learning (ML), which is an interdisciplinary subject and approach [40, 41], has been applied in various research areas, e.g., image detection [42] and manufacturing. ML has also been found to be an effective approach for atmospheric research, e.g., cloud parameter retrieval [43] and numerical weather prediction [44]. Methods such as neural network (NN) have also been applied to RT calculations, especially for approximating solar irradiance [45, 46, 47]. These models employ ML to learn the relationship between atmospheric parameters (as well as surface and incident solar information) and radiances or irradiances [45, 48]. Input data for ML models are normally essential parameters in the Earth-atmosphere system, e.g., atmospheric, cloudy, surface, and solar variables, because they all have significant influences on RT processes. However, these parameters are often of different dimensions and with different variations, which renders the data training, i.e., ‘learning’, difficult.

Unlike the aforementioned ML RT models that use atmospheric parameters to estimate radiances, this study introduces a NN-based fast HRT model where the training is performed in the radiance domain. A small number of representative accurate RT simulations is performed, and the resulting radiances are used as inputs for the NN model to calculate the full hyperspectral radiances. The paper is organized as follows. The general procedure and idea for the NN HRT model is introduced in Section 2. Section 3 compares results given by the NN and PCA HRT models, and Section 4 summarizes conclusions from this study.

2.2 Methods

Accurate HRT models use a LBL approach, in which rigorous RT simulations are performed independently for each wavenumber/wavelength; the computational burden is therefore proportional to the number of wavenumbers/wavelengths needed.

Due to the spectral variation of gaseous absorption, high spectral resolution is required for the RT calculations. On the other hand, the information content of a spectrum is typically much smaller than the number of absorbing lines. This implies that radiances at different wavelengths should be correlated to each other to some degree. This principle has been used in the development of the fast PCA HRT model by [38], which uses radiance training data to calculate PC vectors and then uses a linear combination of a limited number of PC vectors to approximate radiances across the whole spectral range.

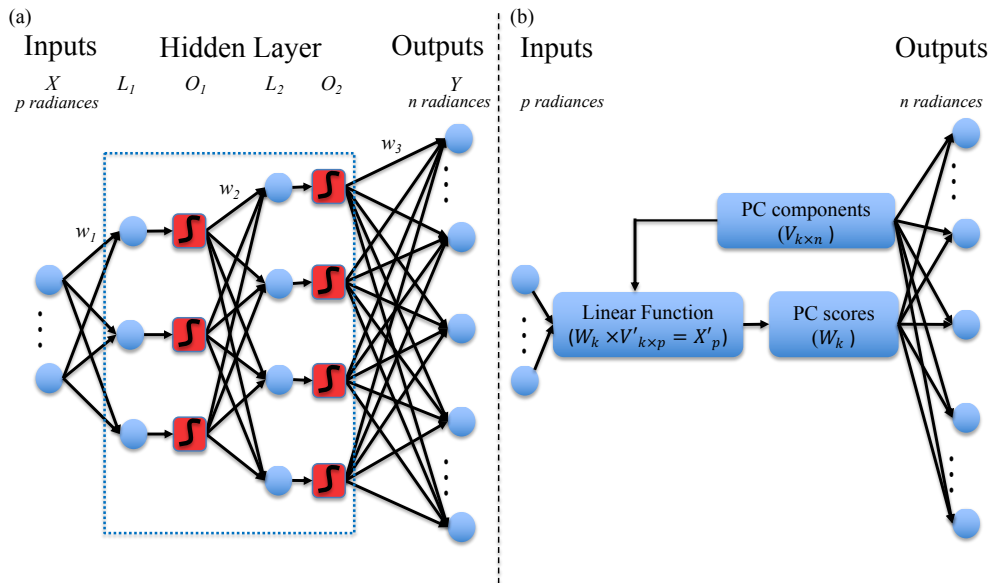


Figure 2.1: Schematics of the Neural-network (NN) based and principal component analysis (PCA) based models for fast hyperspectral radiative transfer simulations.

We first introduce the PCA model [16, 38] that will be used to evaluate our ML model. The right panel of Fig.2.1 is a schematic of the PCA HRT model. If we have radiances at n monochromatic wavelengths for m atmospheric scenarios as our training set $X_{m \times n}$, the first k PC vectors of $X_{m \times n}$ can be given as $V_{k \times n}$. The PCA model uses these k PC vectors to approximate any new X_n using the weights W_k of each PC vector (i.e., PC scores). To get the PC scores W_k , only p radiances X'_p within the spectrum are calculated using rigorous RT simulations (p is normally much smaller than n , but larger than k , i.e., $k < p < n$) according to the following formula:

$$W_k \times V'_{k \times p} = X'_p \quad (2.1)$$

$V'_{k \times p}$ is a subset of $V_{k \times n}$ obtained by choosing values for the appropriate p channels.

Since $V'_{k \times p}$ is not a square matrix, we use the pseudoinverse $(V'_{k \times p})^+$ to find the least squares solution of Eq. (2.1); the dimension of this pseudoinverse matrix is $p \times k$. Then, we have:

$$W_k \approx X'_p \times (V'_{k \times p})^+ \quad (2.2)$$

Hence, the full spectral matrix X_n (here it is a $n \times 1$ vector) can be calculated by:

$$X_n = X'_p \times (V'_{k \times p})^+ \times V_{k \times n} \quad (2.3)$$

which, in principle, is a linear combination of inputs (X'_p), which can be given by any monochromatic RT model for the given atmospheric scenario.

However, the gas absorption coefficients are highly nonlinear functions of wavelength. Thus, the linearity between radiances at different wavelengths may not always be satisfied, and it may be more reasonable to develop a non-linear transformation from X'_p to X_n for fast HRT models.

This study focuses on the procedure of extending a small number of radiances to a larger number of hyperspectral radiances based on a ML technique; we use neural network (NN) as an example. We employ pre-calculated or observed radiance datasets (i.e., $X_{m \times n}$ as discussed above) directly; the basic RT calculations themselves will not be discussed here. The actual observational data is from the OCO-2 measurements, and the synthetic hyperspectral radiance dataset is from [49]. The efficiency gained by applying the NN or PCA model can be simply expressed as the ratio of the total number of required radiances to the number of channels or monochromatic wavelengths needed for the prediction (i.e., n/p).

We use NN to find a non-linear relationship between radiances at the selected channels and those on the entire spectral grid. The goal here is to demonstrate the difference between the PCA and NN models. In this context, it is important to use the same set of channels for the two models. For the sake of simplicity, we select channels (for both NN-based and PCA-based models) using an equally-spaced grid. Optimizing the channel selection will be the subject of future research. The inputs for the NN (essentially a nonlinear regression model) are radiances at a selected fraction of channels; the outputs are NN predictions for the entire wavelength range. According to the universal approximation theorem [50, 51], a feed-forward NN with a single hidden layer is already good enough to approximate continuous functions on compact subsets of high-dimensional real space. This theorem shows the capability of the NN to perform non-linear regression with non-linear activation functions. We

use a fully connected three-layer NN model (the choice of three layers is based on hyperparameter optimization and computational efficiency considerations); the NN structure is shown in the left panel of Fig.2.1. The input layer consists of p neurons, i.e., the set of input spectral radiances. L_1 and L_2 are the hidden layers, consisting of p_1 and p_2 neurons respectively. Y is the third/output layer consisting of n neurons, i.e., the radiances over the entire spectral region. Note that in the schematic the bias unit is not shown; this is an extra neuron added to each hidden layer that has a value of 1.

The following five equations (in matrix form) illustrate how NN works.

$$L_1 = W_1 X \quad (2.4)$$

$$O_1 = f_1(L_1) \quad (2.5)$$

$$L_2 = W_2 O_1 \quad (2.6)$$

$$O_2 = f_2(L_2) \quad (2.7)$$

$$Y = W_3 O_2 \quad (2.8)$$

Here, X stands for the input parameter, and W_1 , W_2 , and W_3 are the synaptic weights of hidden layer 1, 2, and the output layer respectively. f_1 and f_2 are the activation functions for each hidden layer. L and O are the input and output of the hidden layer, respectively. Y is the output. The nonlinearity of the NN arises from the usage of the nonlinear activation function. If f_1 and f_2 are both linear activation functions, the whole system is still linear. Nonlinear activation functions are preferred since they allow the NN to find more complex structures in the data.

The logistic function (sigmoid) and hyperbolic tangent function (tanh) are popular activation functions for the NN. However, if the input value of the activation function is extremely small or large, their derivatives would be close to zero. Thus, it becomes difficult to update the weights due to the problem of “vanishing gradients”. In our NN, we use the Rectified Linear Unit (ReLU) as the activation function to avoid the vanishing gradients problem [52]. Furthermore, compared to the expensive operations (e.g., exponentials) of sigmoid and tanh, the ReLU function is

computationally more efficient and can therefore accelerate the convergence rate for the training.

We also need to choose the loss function (henceforth annotated Δ) and the optimization algorithm. To minimize the absolute difference for channel radiances, Δ is defined as the mean absolute error (MAE):

$$\Delta = \frac{\sum_i |true(i) - pred(i)|}{n}, i = 1, 2, \dots, n \quad (2.9)$$

Here, n is the total number of total channels within the band and i is the channel index. The choice of the optimizer will be discussed in Section 2.3.

There are also other parameters for NN training, such as dimensions of the hidden layers and the corresponding neuron numbers (i.e., p_1 and p_2). However, there is no unique formula that dictates how to choose them for HRT radiance simulations. We consider parameter sweep, based on the rate of convergence as well as the value of the loss function to perform hyperparameter optimization of p_1 and p_2 . The optimal parameters for the four NNs trained in this study are reported in Table 2.1. The first three models represent OCO-2 band observations in the O₂-A, strong CO₂, and weak CO₂ bands, each of which include 1016 independent channels. Observations from polar orbiting satellites provide global coverage and thereby constitute a thorough and complete dataset for NN training. Observations from 50,000 atmospheric scenarios are used as the training set, and 20,000 other scenarios are chosen for validation. We also consider simulated monochromatic reflectances between 0.75 and 0.92 μm (at a spectral resolution of 0.05 cm^{-1} for a total of 50,000 wavelengths) for the fourth NN test; these RT simulations account for gaseous absorption, and scattering by air molecules and aerosols. We use an atmospheric profile dataset developed by the Copernicus Atmospheric Monitoring Service (CAMS) of the European Centre for Medium Range Weather Forecasts (ECMWF), which is a collection of representative model atmospheres [53]. The profiles are on a 60-level vertical grid from the surface to 0.1 hPa, covering realistic annual and diurnal variations in temperature, specific humidity, and the mixing ratios of ozone, carbon monoxide, nitrogen dioxide, sulfur dioxide, and formaldehyde. For this case, we use 5,000 atmospheric scenarios as the training set and another 2,000 scenarios for validation. More details can be found in [49]. Note that the training and RT models presented in this study are independent of the spectral response function. For the OCO-2 cases, the prediction is directly performed from selected instrument channel radiances to radiances on the full channel grid. For the monochromatic

radiance case, it is done from selected monochromatic radiances to the full set of monochromatic radiances over the entire wavelength range. This indicates that the ML and PCA procedures can be applied both for channel-based radiances and for monochromatic radiances.

	Number of scenarios	Number of channels (N)	P_1	P_2
O ₂ -A band	70,000	1,016	50	200
CO ₂ Strong band	70,000	1,016	50	200
CO ₂ Weak band	70,000	1,016	50	150
Monochromatic RT simulations	7,000	50,000	500	6,000

Table 2.1: Parameters of the NN-based model for the four cases considered in this study, including the number of scenarios used for training and validation, total number of channels, and dimensions of the hidden layers. The MAE and ReLu are used as the loss and activation function, respectively, and Adaptive Moment Estimation (AdaM) is used as the optimizer.

To improve NN performance, scaled variables are used for data training, so that all input parameters are of similar magnitude. In this study, we perform the data transformation according to Eq.(2.10) using the mean over the training dataset for the channel of interest and the mean of the specific input parameter over the selected p channels.

$$input(i, j) = \frac{original(i, j)}{channel_{mean(j)} \times mean(original(i, :))} \quad (2.10)$$

Here, i and j are the indices for the scenarios and selected input channels, respectively.

We implement our NN in Keras, a high-level NN application programming interface (API) written in Python. It is capable of running on top of TensorFlow, and can run on both central processing unit (CPU) and graphics processing unit (GPU). On average, the model performs 2000 iterations over entire training sets (e.g., 50,000 scenarios \times 1016 channels) within less than 10 minutes on a NVIDIA TITAN Xp GPU, i.e., < 0.3 seconds per iteration over 50 million channel computations.

Once the PCA-based and NN-based HRT models are trained, the computational time for both models is proportional to the number of selected input channels, since the prediction takes negligible time (more than 99% of the time is spent on computing the radiances).

2.3 Results

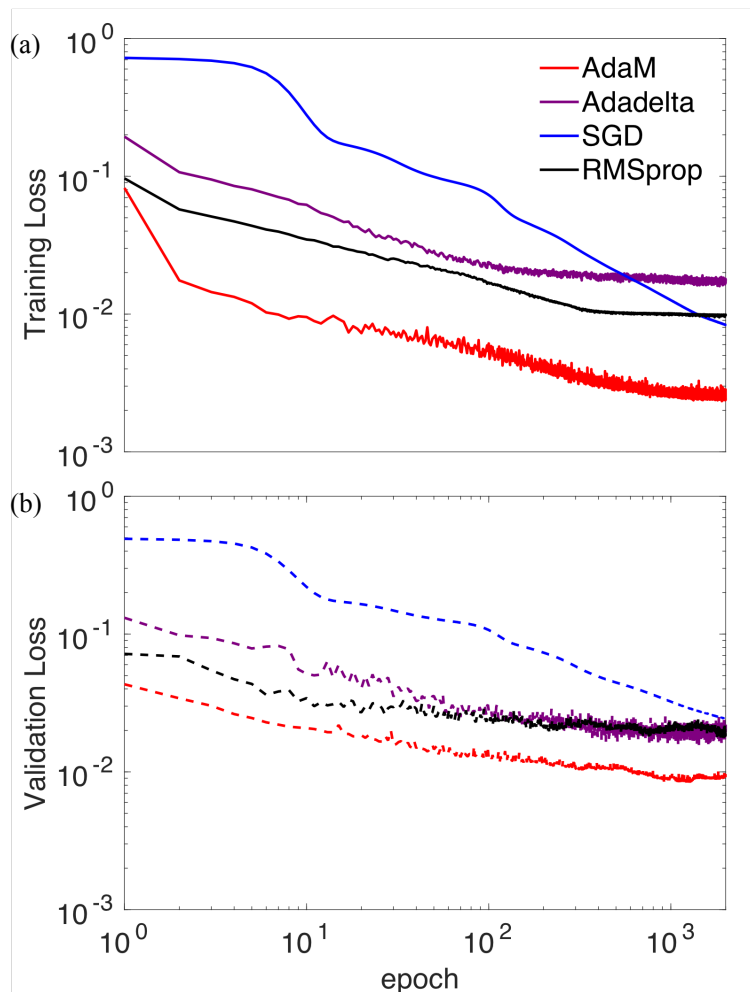


Figure 2.2: (a) Training and (b) validation losses of the four different optimization algorithms for simulations of the OCO-2 O₂-A band radiances.

We compare the performance of four widely used optimizers for the minimization of Δ , i.e., Stochastic Gradient Descent (SGD), Root Mean Square Propagation (RMSprop), Adaptive Moment Estimation (AdaM), and Adadelta [54]. SGD is an iterative method based on a stochastic approximation of gradient descent optimization. Adadelta is an algorithm for gradient-based optimization using adaptive learning rates; large (small) learning rates are dynamically chosen for parameters associated with infrequent (frequently occurring) features. RMSProp is similar to Adadelta, except for a slightly different parameter update rule [54]. AdaM combines the ability of Adadelta to deal with sparse gradients and that of RMSProp to handle

non-stationary cases. AdaM can be easily implemented, requires little memory, and is well suited for problems that are large in terms of data size [55]. Fig.2.2 illustrates the training and validation loss given by the four optimization algorithms for the same OCO-2 O₂ A-band radiance dataset. Although both training loss and validation loss of the four algorithms reach steady states after 2000 iterations, clear differences are discernible. The best performance is achieved by the AdaM algorithm, which has the largest convergence rate and smallest loss for both the training and validation datasets. AdaM also works well for the other datasets we considered in this study. Therefore, we choose AdaM as the NN optimizer for all simulations.

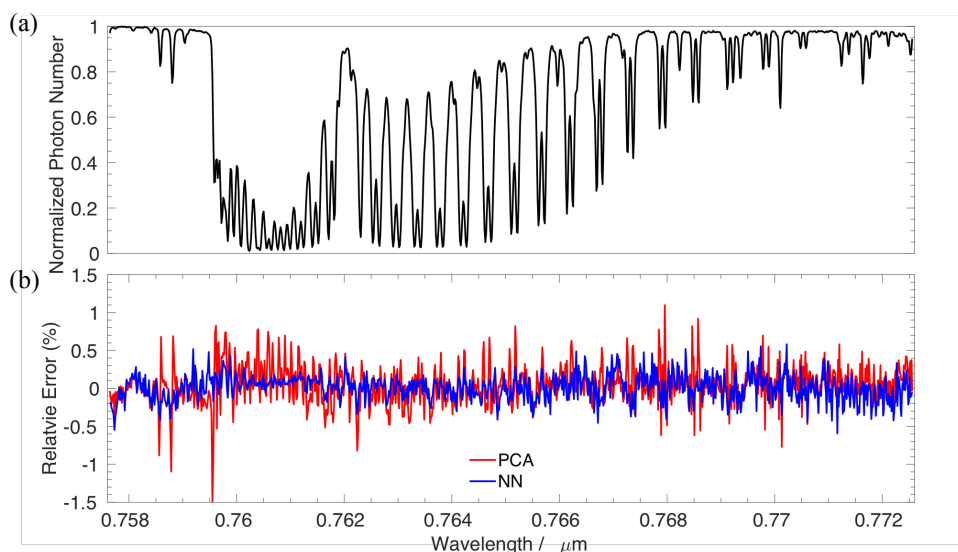


Figure 2.3: (a) Sample OCO-2 O₂ A-band observation; (b) Accuracy of PCA-based and NN-based HRT simulations using 50 channel radiances as inputs. The normalized photon number is defined as the ratio of the photon number to its maximum value over the entire spectral range.

Fig.2.3 compares the accuracy of NN-based and PCA-based HRT simulations for a sample OCO-2 O₂ A-band observation. The relative errors (REs) are calculated as defined in [13], i.e., relative to the largest value over the entire spectral region. The top panel shows a radiance spectrum; we use 50 equally-spaced observations to predict the radiances in all 1016 channels. The REs of the two fast HRT methods are given in the bottom panel. Both methods result in REs less than 0.5% for most channels, with only a few PCA-based results having REs around 1%. The mean absolute REs of the NN-based and PCA-based results are 0.5% and 0.6%,

respectively. Note that, if simulated monochromatic radiances, (instead of channel-averaged radiances), are used, the errors for channel radiances (integrated over channel response functions) will be even smaller (similar to the treatment presented by [16]).

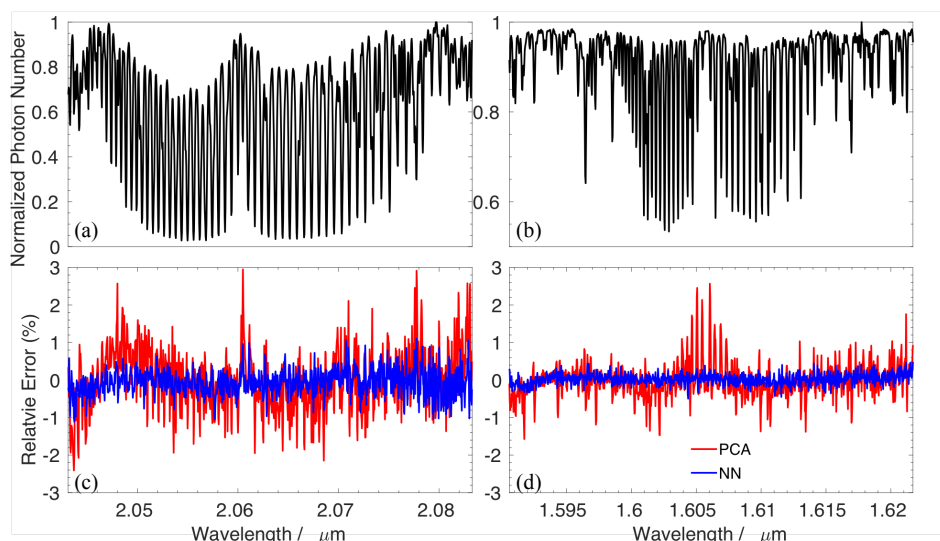


Figure 2.4: Same as Fig.2.3 but for the two CO₂ absorption bands measured by OCO-2.

Fig.2.4 is similar to Fig.2.3 but for the two CO₂ absorption bands measured by OCO-2. Again, both the NN-based and PCA-based methods provide accurate results, with maximum REs are less than 1% and 3%, respectively. Overall, the NN-based results for all three OCO-2 bands are slightly better than those given by the PCA-based model.

The NN-based and PCA-based methods discussed here use a small fraction (5%, using 50 channels out of 1016 for the examples in Figs.2.3 and 2.4) of channel radiances to predict radiances over the entire hyperspectral range. There is, of course, a balance between the computation burden and accuracy depending on the number of input radiances used for the prediction. The accuracy increases with the number of input radiances/channels, but at the cost of more independent RT simulations.

Fig.2.5 shows the mean absolute relative errors of the two HRT models over 20,000 atmospheric scenarios as a function of the number of input channels (N). Overall, the

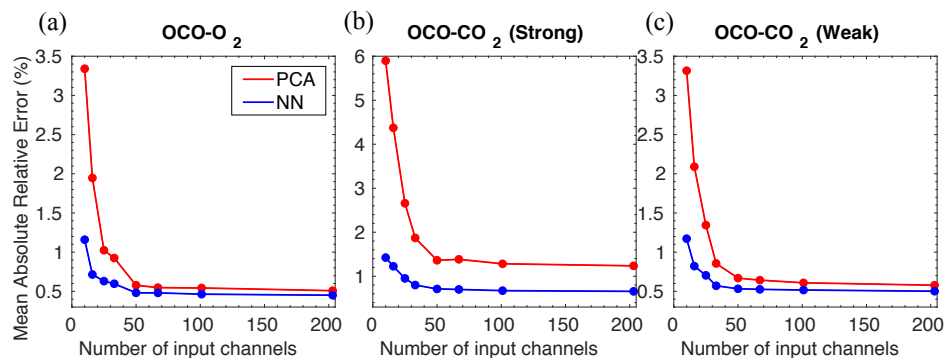


Figure 2.5: Mean absolute relative errors given by the PCA-based and NN-based fast HRT models as a function of the number of input channel radiances. The results are ensemble averaged over 20,000 tests.

NN-based model gives smaller mean errors compared to the PCA-based simulations, especially for models with small numbers of channel. As expected, the mean errors given by both methods decrease initially as more channels are included. However, a plateau is reached when N is around 50–100. This indicates that there is a lot of redundancy in the spectral information. LBL simulations for each of the 1016 channels are not necessary; instead, only 5% of those channels require simulations, with results for the rest obtained using NN-based or PCA-based simulations. Another advantage of the fast HRT models discussed here is that they can be easily coupled with LBL RT simulations or other fast RT models that directly solve the RT equations.

Fig.2.6 shows a comparison of the NN-based and PCA-based HRT models for simulation of radiances at 50,000 monochromatic wavelengths between 0.75 and 0.92 μm . The NN-based HRT model introduces maximum REs less than 0.3%. On the other hand, the PCA-based HRT model has large errors (5%) at several wavelengths, with most of them corresponding to intermediate absorption features (gas absorption optical depth between 1–10). Note that we calculate radiances at 200 wavelengths to predict 50,000 radiance values over the entire grid, i.e., only 0.4% of full LBL RT simulations are needed for the NN or PCA models; this results in a speedup of 250 compared to rigorous LBL simulations.

Fig.2.7 shows cumulative probability distributions of spectrally averaged REs, maximum REs and mean of largest-500 REs over 2000 validation scenarios. Over 90% of PCA-based HRT results have mean REs less than 0.15% while over 80% of NN-based HRT results have similar errors, which is slightly worse than the PCA-based

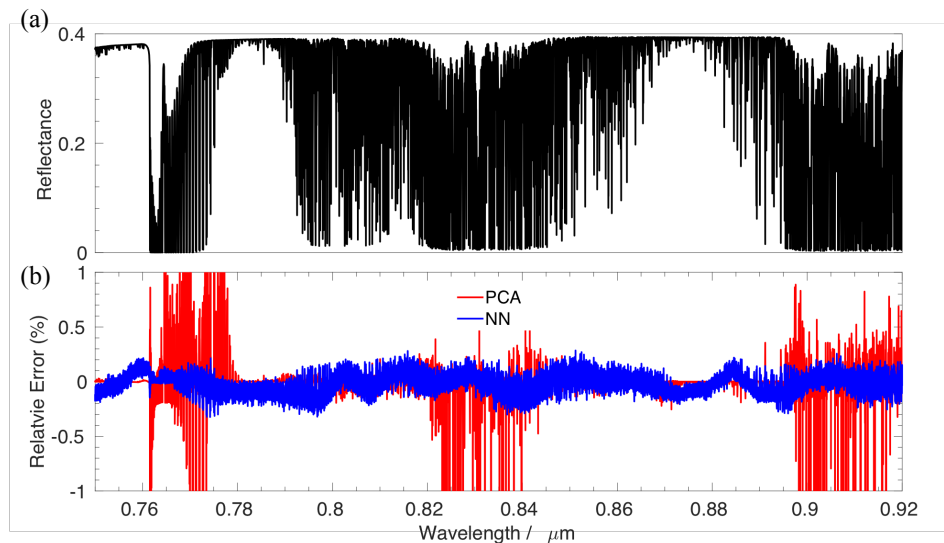


Figure 2.6: Same as Fig. 2.3 but for monochromatic RT simulations over the solar spectral range from 0.75–0.92 μm .

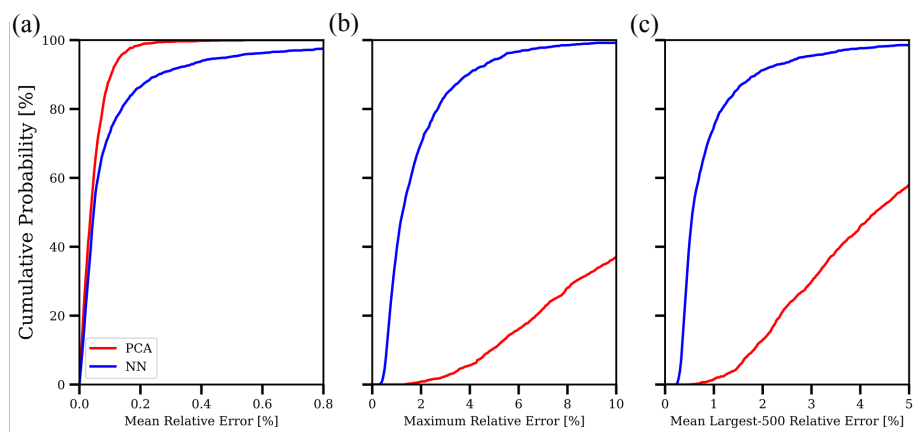


Figure 2.7: Cumulative probability distributions of (a) spectrally averaged mean absolute REs, (b) maximum REs and (c) mean largest-500 REs for 2,000 atmospheric scenarios.

results. However, for maximum absolute REs and mean largest-500 REs, the PCA-based results are much worse than NN-based results. Overall, the NN-based HRT's results are more robust, perhaps because the NN model enables deeper learning and approximation of the nonlinearity between channel radiances, especially for the intermediate to strongly absorbing channels where the PCA-based HRT model is less effective.

2.4 Conclusions

This study introduces a NN-based fast RT model for hyperspectral radiance simulations. The NN is tested for both synthetic (monochromatic) and observed (channel-averaged) radiances; the excellent results indicate that ML techniques have great potential for fast HRT model development. By providing relationships between different radiances (that have the same dimension), rather than between atmospheric variables (temperature, gas profiles) and radiances, our model makes the NN training easier and more robust. Compared with a PCA-based model, the NN-based model provides higher accuracy for OCO-2 simulations when the same fraction of radiances is used for the 'prediction'.

The ML technique shows great promise for fast HRT simulations. However, several questions naturally arise from our results. First, to what extent can we identify redundant information in our input data? Fig.2.5 implies that only a small fraction of input channels is necessary for accurate radiance prediction. However, it is important to keep in mind the training process as well. This process identifies patterns and features that allow the NN to perform effective predictions from limited information. Hence, the apparent compression given by the model is only possible when the NN can first identify the patterns in the data. This pattern recognition is precisely what occurs when the NN interacts with the training data. We know that similar data would also be effectively compressed by the NN. However, input data that is too far from what the network was trained with may produce less accurate predictions. This issue has nothing to do with our approach, but is instead a fundamental problem in ML (see, e.g., [56]). Future advances in the field are likely to improve the ability of NNs to generalize to situations beyond those they were trained on.

Second, is it possible to quantitatively assess the requirements for future measurement protocols such that the compression illustrated in Fig.2.5 can be exploited? In other words, under what circumstances could we use lower resolution measurements to make similarly accurate predictions? This is a difficult and subtle question, since

it cuts to the core of ML theory. In lieu of new frameworks in this area, one could attempt to synthesize artificial datasets with which the NNs could be tested. In principle, one could track the prediction accuracy as a function of distance from training data and find out the point at which the NN fails due to it being 'out of its depth'. This could also be carried out by another NN, using the rapidly-growing approach of generative adversarial networks (GANs).

For remote sensing and assimilation problems, the RT models are also required to provide Jacobians (i.e., partial derivatives of radiances with respect to atmospheric temperature, gas concentration, and other parameters); the NN-based model may also accelerate such calculations. For this purpose, here we briefly explain how to calculate Jacobians in the NN-based HRT model. Assume that input variables and model predictions are denoted as x_i and y_j , respectively, and we want to calculate the Jacobians with respect to variable ξ . According to the chain rule for multi-variable functions (i.e., $\frac{\partial y_j}{\partial \xi} = \sum_i \frac{\partial y_j}{\partial x_i} \times \frac{\partial x_i}{\partial \xi}$). The partial derivative term between the NN input and prediction $\frac{\partial y_j}{\partial x_i}$ can be pre-calculated and saved in a LUT. The $\frac{\partial x_i}{\partial \xi}$ term can be directly calculated by the RT model (e.g., LIDORT [57]).

The accuracy and structure of the NN-based model make it amenable to coupling with existing fast RT models (e.g., CRTM [58], RTTOV [59], and ARMS [60]) to further improve computational efficiency. This study is only intended to present representative examples of the method. In order to reach the full potential of such ML-based approaches, more effort is required to optimize the training procedure and hyperparameter selection; this will be the subject of future studies. Further, equally spaced channels were employed in this study; using radiances from a more representative unequally spaced wavelength grid could conceivably improve model performance. Future studies are also envisaged to test and extend the models to wider spectral ranges and for scenarios with more complicated atmospheric temperature, gas, aerosol, and cloud structures.

*Chapter 3***EVALUATION OF MODELED HYPERSPECTRAL INFRARED SPECTRA AGAINST ALL-SKY AIRS OBSERVATIONS USING DIFFERENT CLOUD OVERLAP MODEL**

T. Le, V. Natraj, H. H. Aumann, Y. L. Yung "Evaluation of modeled hyperspectral infrared spectra against all-sky AIRS observations using different cloud overlap model", *in prep*

3.1 Introduction

Clouds and their feedbacks play a fundamental role in climate change (see, e.g., [61, 62, 63, 64]). Advancements in hyperspectral infrared sounding have provided us with a rich dataset of daily global radiance measurements since the turn of the century, with information content to sense cloud properties. The Atmospheric Infrared Sounder (AIRS) is a hyperspectral infrared sounder on board NASA's Aqua satellite in sun-synchronous orbit [19] that makes more than two million observations each day. The atmospheric state (profiles of temperature, humidity, trace gas concentration, and cloud parameters) can be retrieved from the radiance spectrum, which can then be used in weather forecasting [65].

However, data from hyperspectral infrared sounders appear to be underutilized for the study of clouds. One of the reasons for this is that modeling cloud radiative transfer (RT) effects is complicated since clouds reflect solar radiation and emit longwave radiation. Further, the radiative effect of clouds depends on the cloud altitude, type, particle size and overlap details [66, 67]. Another reason is that for use in data assimilation, RT require a combination of sufficient accuracy, efficiency, and Jacobian, tangent-linear and adjoint model capability.

Uncertainties in RT modeling of cloudy atmospheres arise not only from lack of adequate knowledge of the cloud optical properties, but also because the vertical distribution of liquid and ice clouds is not known. The vertical cloud distribution is modeled by making assumptions about cloud overlap. Typical cloud overlap assumptions include maximum, random and maximum-random overlap. Geer et al. 2009 developed an average overlap scheme for microwave radiative transfer which is weighting by the hydrometeor [68]. In all cases, radiances are computed for several

atmospheric “columns”, with the effective radiance calculated using a weighted average of the individual column radiances. The columns are constructed from the horizontal cloud fraction at each atmospheric level (which is assumed to be known). Different overlap assumptions then determine how the cloudy layers are stacked in the vertical. In the case of maximum overlap, all the cloudy layers are concentrated in the same columns as much as possible. For random overlap, the cloudy layers are distributed randomly across the columns. Maximum-random overlap assumes that the cloudy columns are maximally overlapped in adjacent vertical layers that are both cloudy, but randomly distributed where there is a cloud-free layer in between.

The drawback of the maximum and random overlap methods is that they are based on geometric assumptions that are too simplified to handle multi-layered clouds [69]. Maximum-random overlap, on the other hand, is more realistic; however, about 10–100 columns are required to accurately represent typical cloudy atmospheric scenarios [70]. Therefore, using the maximum-random overlap assumption significantly increases the runtime of RT models, necessitating the use of fast and accurate cloud overlap methods. Hydrometeor-weighted average overlap approach has been shown can reduce the errors by 40% in areas of cloud and precipitation [68] by using only two columns.

Recent studies have made great progress in using all-sky microwave and infrared radiances assimilation [71, 72]. Geer et al. 2019 tested a multiple independent columns approach under maximum-random overlap assumption in RTTOV model (Radiative Transfer for TOVS) [72]. However, this approach is computationally demanding. The cost is about 34 times more than clearsky radiative transfer in the ECMWF system. Therefore, we need to find a balance between the computation burden and accuracy for all-sky infrared radiance assimilation. In this study, we evaluate the Community Radiative Transfer Model (CRTM) with four different cloud overlap schemes.

In order to evaluate CRTM performance for all-sky radiance simulations, we simulate tens of thousands of scenarios and compare against AIRS observations by looking at the probability distribution function of the difference between the surface temperature (obtained from European Centre for Medium-Range Weather Forecasting (ECMWF) model estimates) and the brightness temperature (T_B) in several atmospheric window channels. This difference is a measure of the radiometric effect of clouds. Aumann et al. 2018 used Pearson correlation of T_B histograms to evaluate RT model performance [73]. However, this is not an ideal approach to

compare probability distributions, as will be discussed in Section 2.4. Here, we utilize a statistical metric, called Wasserstein distance, to quantitatively measure how far model probability distributions deviate from AIRS observations. Compared to simple correlation techniques, the Wasserstein distance is less sensitive to the choice of histogram bins and provides a better characterization of the overall shape of the distribution. We also perform the model-observation comparison on 846 selected AIRS channels between 790 cm^{-1} to 1231 cm^{-1} .

The paper is organized as follows. In Section 2, we describe the dataset and relevant models used in this work. We also introduce the Wasserstein distance statistical metric, which is used for our model-measurement inter-comparison. Section 3 first summarized the day/night and different latitude regions for more than 80 thousand cases we used in this study. Then we evaluate all-sky CRTM simulated radiances under different cloud overlapping schemes against AIRS observations. Finally, we summarize our major findings in Section 4.

3.2 Relevant datasets and methods

3.2.1 AIRS

AIRS is a grating array spectrometer covering the thermal infrared and shortwave infrared spectral range with 2378 channels. The instrument spectral resolving power is $\frac{\nu}{\delta\nu} = 1200$. The noise is typically smaller than 0.2 K. The nadir footprint of AIRS is 13.5 km from a 705 km orbit, with scans of about ± 49.5 degrees from nadir [19]. AIRS observations in the infrared region enable the atmospheric temperature and water vapor vertical profile retrieval.

We used AIRS observations within 12 hours between 2018/10/31 21:00 UTC to 2018/11/01 21:00 UTC. The land or frozen oceans cases are excluded to avoid the possibility of introducing additional surface effects since they are difficult to accurately calculate the surface albedos. We only use non-frozen ocean cases (82,271 cases) in this study, more details can be found in Table 1.

3.2.2 ECMWF

The model profiles are generated by the ECMWF operational global weather forecasting system [74]. The best available estimate of the atmospheric state is taken from a combination of short-range forecast and analysis observational information (such as satellite radiances, satellite-retrieved atmospheric motion vectors, near-surface wind vectors from scatterometers, Global Navigation Satellite System radio-occultation measurements, and so on). The original ECMWF atmospheric states

are estimated using 3 hours and 0.25° horizontal resolution (25 km at the equator) time/space interpolation, which created a matchup error for the comparison with AIRS observations [73]. In study, ECMWF provided a higher time/space interpolation estimation by the ECMWF internal 15 minutes and 9 km operational ingest system. For 82,271 non-frozen ocean AIRS observations from 2018/10/31 21:00 UTC to 2018/11/01 21:00 UTC, we get atmospheric state profiles at 137 vertical levels for these cases, including pressure, temperature, O₃, H₂O, liquid/ice cloud content and cloud cover. All AIRS observations and ECMWF vertical profiles used in this study can be downloaded from <https://airsteam.jpl.nasa.gov/ftp/hha/ECMWF20181101/>.

3.2.3 Community Radiative Transfer Model

The Community Radiative Transfer Model, CRTM is a fast-radiative transfer model developed by the Joint Center for Satellite Data Assimilation in the United States [75]. The CRTM simulates satellite infrared and microwave radiances with respect to the atmospheric state variables (e.g., temperature, pressure, humidity, water and ice cloud content, trace gas concentrations). It consists of the following key modules: gaseous transmissions, surface emission and reflection, cloud and aerosol absorption and scattering, and radiative transfer solver. The default radiative transfer algorithm used for scattering calculation is the Advanced Doubling-Adding (ADA) algorithm. CRTM also contains a k-matrix module for Jacobian calculations, tangent-liner module and adjoint module, which are important in the radiance assimilations and inversion part in retrieval problems [76, 77, 72, 78].

In this study, we use CRTM version 2.4.0. Its cloud module has six cloud types: water, ice, rain, snow, graupel and hail which defined by the cloud particle densities. We only use water and ice clouds in our calculations. The cloud optical properties (i.e., mass extinction coefficient, single-scattering albedo, and asymmetry factor) data we used in this study is the default CloudCoeff.bin (version 3.0.4). The ice cloud optical properties of this version are based on MODIS collection 5 ice model [79].

The CRTM also requires cloud particle effective radius vertical profile. To obtain the effective radius, we use equation (2) in [80] for water clouds, and temperature-depended equation from [81, 82] for ice cloud. Four cloud overlapping schemes (i.e., Maximum overlap, random overlap, maximum-random overlap, and average overlap) are available in CRTM for all-sky radiation calculations [83]. They use

two-column radiance approach, which can be expressed by the following formula.

$$R = (1 - tcc) \cdot R_{clr} + tcc \cdot R_{cld} \quad (3.1)$$

where R_{clr} is the clear sky Top Of the Atmosphere (TOA) radiance, R_{cld} is the cloudy sky TOA radiance where both water and ice cloud are included and tcc is the total cloud fraction. To be noticed, the value of R_{cld} and tcc are both depend on the selected cloud overlapping scheme. Maximum-random overlap scheme in CRTM only use two columns, any this may reduce its accuracy compare with using more columns.

The CRTM calculated radiance spectra for all two sub-columns and then averaged to obtain the simulated AIRS radiances using ECMWF temperature, cloud, water, and ozone profiles as input. CO2 concentration is fixed using U.S. 1976 Standard Atmosphere profile, but be scaled to 405 ppmv for Year 2018.

3.2.4 Wasserstein Distance

Aumann et al. (2018) use Pearson correlation to compare the model and measurement probability distributions [73]. However, while the Pearson correlation coefficient is a measure of the linear correlation between two variables, it is not suitable for comparing probability distributions. A high degree of correlation does not necessarily imply high causal relationship. For example, for the two distributions shown in Figure 3.1, the Pearson correlation coefficient is 1.0, despite clear differences between the distributions. Instead, we employ the Wasserstein distance, which is a measurement of the distance between two probability distributions.

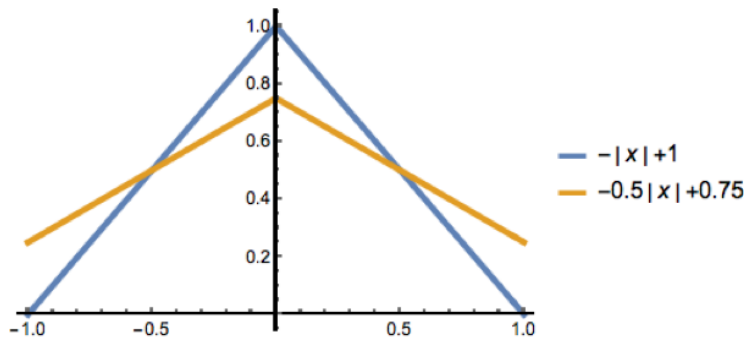


Figure 3.1: Two probability distributions that have a Pearson correlation coefficient of 1.0 and yet are clearly very different.

The Wasserstein distance is used to measure how far away two probability distributions are from each other. The n th Wasserstein distance for two distributions p and

q is defined as:

$$W_n(p, q) = \left(\inf_{\gamma \in \Pi(p, q)} \mathbb{E}_{(x, y) \sim \gamma} [|x - y|^n] \right)^{1/n} \quad (3.2)$$

where $\Pi(p, q)$ is the collection of all possible joint distributions combined with the distributions p and q . For each possible joint distribution $\gamma \in \Pi(p, q)$, we calculate the expected value of the distance of all pair of samples from p and q . The lower bound is the n^{th} Wasserstein distance.

The first Wasserstein distance is also known as the Earth Mover’s Distance (EMD), which has important applications in the field of computer science [84, 85]. Intuitively, if one thinks of two probability distributions as two different ways of piling up a certain amount of dirt, then EMD is the minimum cost of turning one pile into the other, where cost is assumed to be the product of the amount of dirt moved and the distance by which it is moved.

For discrete distributions, the first Wasserstein distance can be calculated using the following formula:

$$W(p, q) = \inf_{\forall f} \frac{\sum_{i=1}^M \sum_{j=1}^N d_{ij} f_{ij}}{\sum_{i=1}^M \sum_{j=1}^N f_{ij}} \quad (3.3)$$

where d_{ij} is the distance between p_i and q_j , and f is any possible way to move p to q . f_{ij} is the amount that should be moved from p_i to q_j .

The first Wasserstein distance is a natural way to compare two probability distributions where one is derived from the other by making small perturbations.

3.3 Results

	Day	Night	Total
$ \text{lat} \leq 30$	19,537	17,343	36,880
$ \text{lat} \in (30, 60]$	19,263	17,095	36,358
$ \text{lat} > 60$	2,677	6,356	9,033
All	41,477	40,794	82,271

Table 3.1: Summary of all 82,271 non-frozen oceans AIRS observations from 2018/10/31 21:00 UTC to 2018/11/01 21:00 UTC. We denote $|\text{lat}| \leq 30$, $|\text{lat}| \in (30, 60]$, and $|\text{lat}| > 60$ are tropical zone, mid-latitude zone, and polar zone, respectively.

Table 3.1 summarizes the day/night and different latitude regions for all 82,271 AIRS observations. In this study, we denote $|\text{lat}| \leq 30$, $|\text{lat}| \in (30, 60]$, and

$|lat| > 60$ as tropical zone, mid-latitude zone, and polar zone, respectively. The daytime and nighttime cases are roughly balanced in the whole dataset. Both the tropical zone cases and mid-latitude zone cases count for 44% of all 82,271 cases. However, because the majority of high latitude region is covered by ice, only 11% of our cases are in the polar zone. We evaluate the CRTM simulated radiances against observations of all 82,271 cases by setting different day/night conditions and latitude regions.

In this study, we choose three atmospheric window channels (901 cm^{-1} , 1231 cm^{-1} and 2615 cm^{-1}). The first two are in the thermal infrared spectral range while the last one is in the shortwave infrared range (where effects due to reflection and scattering of solar radiation need to be considered). Figure 3.2 shows probability distribution plots of the difference between surface temperature (ST) and channel brightness temperature for AIRS observations (dashed black), CRTM with average overlap scheme (red), CRTM with maximum-random overlap scheme (blue), CRTM with random overlap scheme (green), and CRTM with maximum overlap scheme (orange) in these three channels for non-frozen ocean day and night cases. On each curve, there are 60 points from -30 K to 90 K. with a 2 K temperature interval. The peak of the probability distribution in all infrared channels (i.e., 901 cm^{-1} and 1231 cm^{-1}) are near 5 K, which suggests, relatively little cloudiness or low clouds. We only observe daytime cases in 2615 cm^{-1} channel with negative ($ST-T_B$) values, which show surface reflectance effect. CRTM with average overlap not only successfully simulates the peak of the probability distribution in all scenarios, but are also in reasonably close agreement with the AIRS observations in terms of the overall shape of the distribution. By contrast, CRTM with maximum-random overlap, random overlap, and maximum overlap fail to simulate the distributions. Maximum overlap gives relatively better simulations among these three overlap schemes, with random overlap being the worst.

Table 3.2 summaries the first Wasserstein distances as well as the Pearson correlation coefficients of the simulated radiances in Figure 3.2 against observations. The models with best performance for each scenario in Table 2 are marked in red. To be noticed, smaller first Wasserstein distance or larger Pearson correlation coefficient indicates better agreement with AIRS observations. In most cases, CRTM with the average overlap scheme is shown to give the best simulations as evaluated by both the first Wasserstein distance and the Pearson correlation coefficient. However, daytime 2615 cm^{-1} for all zones is a special case. The Pearson correlation coefficient

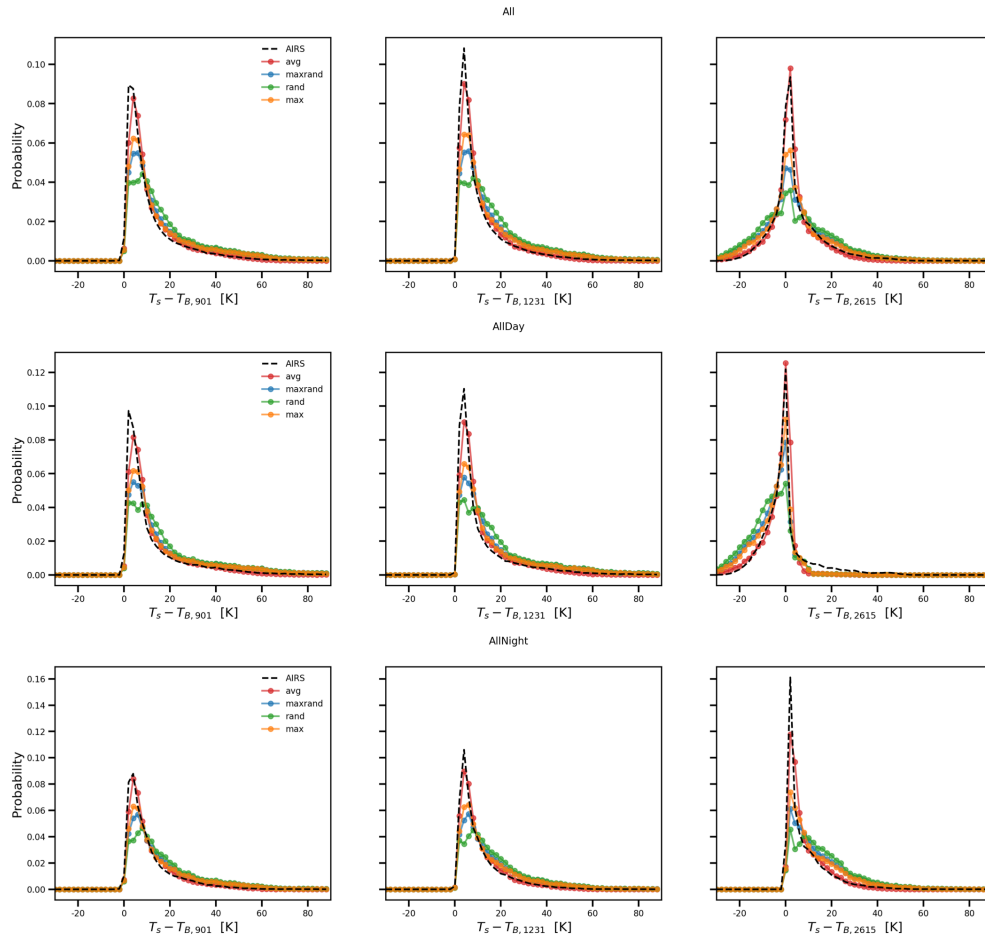


Figure 3.2: Probability distributions of the difference between surface temperature and brightness temperature at three atmospheric window channels. (901 cm^{-1} , 1231 cm^{-1} and 2615 cm^{-1}) for the non-frozen ocean day and night scenarios. The AIRS observations, CRTM with average overlap scheme, maximum-random overlap scheme, random overlap scheme, and maximum overlap scheme results are shown in dashed black, red, blue, green, and orange lines, respectively.

All (Day & Night)						
	901 (Pear- son)	1231 (Pear- son)	2615 (Pear- son)	901 (EMD)	1231 (EMD)	2615 (EMD)
Avg	0.97	0.98	0.99	0.001010	0.001288	0.001009
Maxrand	0.94	0.92	0.93	0.002848	0.003309	0.003016
Rand	0.87	0.83	0.84	0.004107	0.004635	0.004349
Max	0.95	0.95	0.96	0.002268	0.002642	0.002237
Day						
Avg	0.96	0.96	0.95	0.001325	0.001604	0.001829
Maxrand	0.92	0.92	0.94	0.003079	0.003681	0.002643
Rand	0.86	0.84	0.83	0.004238	0.005055	0.005064
Max	0.94	0.87	0.98	0.002283	0.002695	0.003146
Night						
Avg	0.98	0.99	0.94	0.000824	0.001117	0.002043
Maxrand	0.94	0.93	0.84	0.002838	0.003106	0.003727
Rand	0.87	0.83	0.72	0.003974	0.004292	0.004700
Max	0.96	0.96	0.88	0.002202	0.002366	0.003091

Table 3.2: Comparison of performance of CRTM with average overlap, maximum-random overlap, random overlap, and maximum overlap scheme for non-frozen ocean all (day and night), day only, night only scenarios using the first Wasserstein distance. The best performance models for each column are marked in red.

suggests that the maximum overlap scheme is the best in this case, while the first Wasserstein distance votes for the average overlap scheme. From the daytime all zone 2615 cm^{-1} subplot in Figure 3.2, we can easily conclude that the average overlap results (red) match the AIRS observations more closely. The maximum overlap simulations find many more cases with $(ST - T_B)$ between -20 K and -5K, and fewer cases for the peak near 0 K. This suggests that the maximum overlap scheme underestimates the low cloud effects. Hence, this special case indicates that the first Wasserstein distance is more robust than the Pearson correlation coefficient for the comparison between two probability distributions.

Figure 3.3, 3.4, 3.5 are similar to Figure 3.2, but for tropical zone ($|lat| \leq 30$), mid-latitude zone ($30 < |lat| \leq 60$), and polar zone ($|lat| > 60$), respectively. Overall, the average overlap scheme still gives the best simulations among all four cloud overlap schemes. The CRTM with average overlap scheme can provide roughly accurate estimations of the peak and shape of the probability distributions. The model performance is relatively worse in the polar zone compared to the other two zones (Figure 3.5). Although CRTM with all four cloud overlap schemes are able

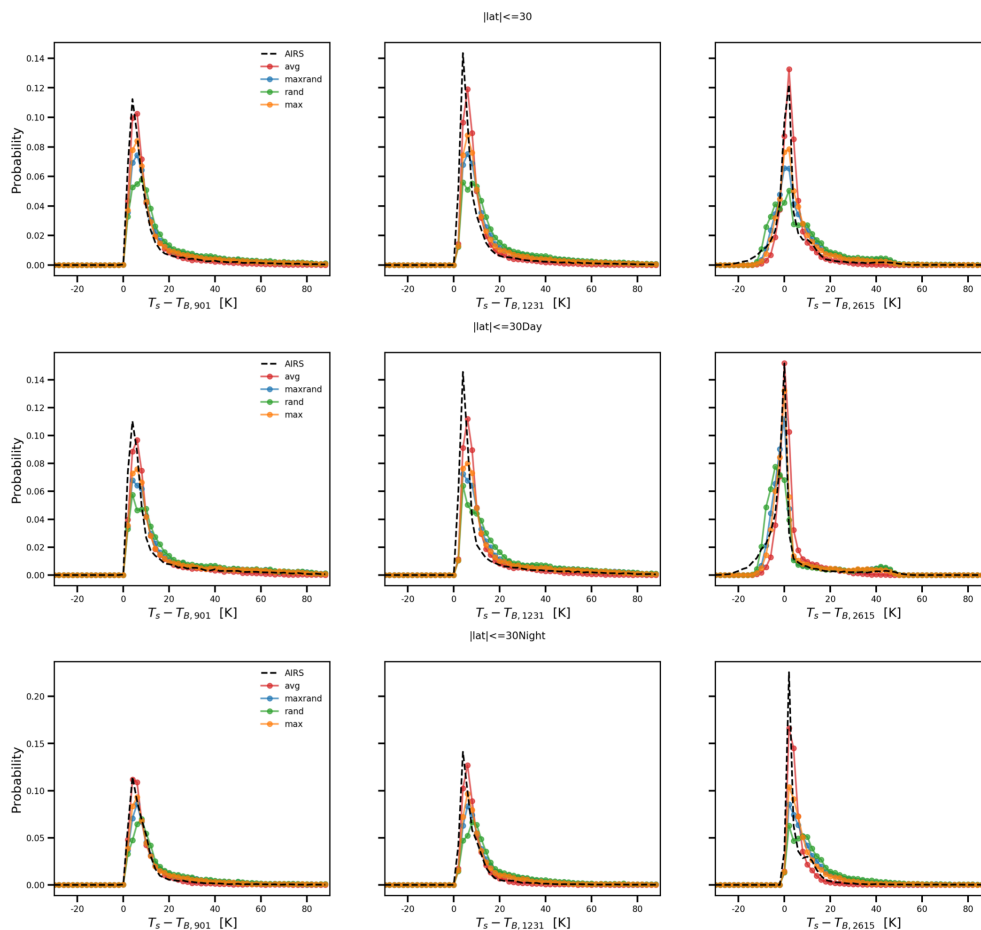


Figure 3.3: Same as Figure 2, but for tropical zone only.

to simulate the two peaks for the daytime case in the polar zone, the secondary peak for daytime 2615 cm^{-1} case has been shifted left for all cloud overlap schemes (for nearly -5 K compared to AIRS observations). CRTM fails to simulate the nighttime case for the polar zone in all three window channels. The simulations are colder than the real AIRS observations.

In addition to these three window channels, we also evaluate the simulated radiances using a wide range of channels that cover CO_2 , H_2O and O_3 absorption regions. Figure 3.6 shows the mean of T_B , mean absolute difference of T_B and the first Wasserstein distance between simulated radiances and AIRS observations for 846 channels between 790 cm^{-1} to 1231 cm^{-1} . The channels with noise level $> 1\text{ K}$ have been removed before calculations. Again, the average overlap simulations are

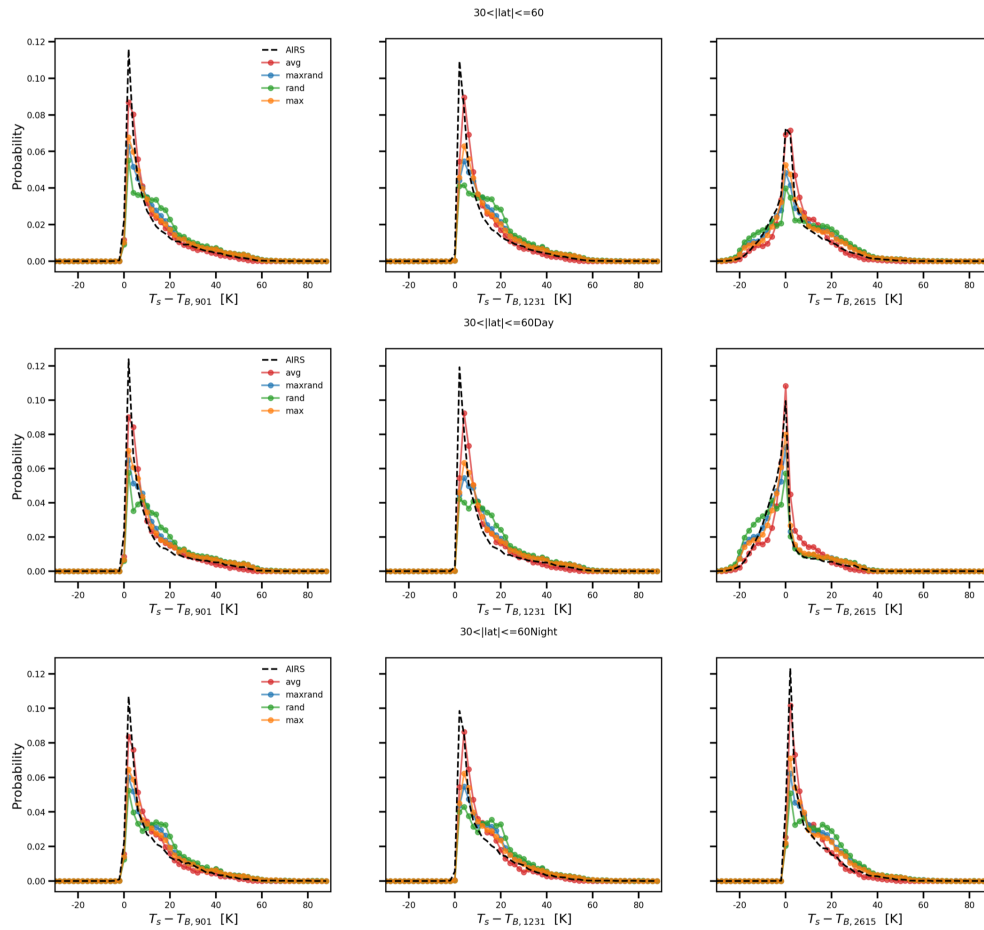


Figure 3.4: Same as Figure 2, but for mid-latitude zone only.

shown to be in reasonably close agreement with observations (the discrepancies are within 0.7 K in terms of T_B) for all 846 channels, including the O3 absorption band around 1040 cm^{-1} .

Figure 3.7 illustrates the pairwise comparison of the observed AIRS 901 cm^{-1} brightness temperature with the CRTM average overlap scheme simulations on a global map. In general, the simulated radiances agree well with AIRS radiances on a global scale, the absolute difference is less than 2 K in most cases. However, it shows a clear regional pattern, especially for the Intertropical Convergence Zone (ITCZ) where the absolute difference can be greater than 30 K.

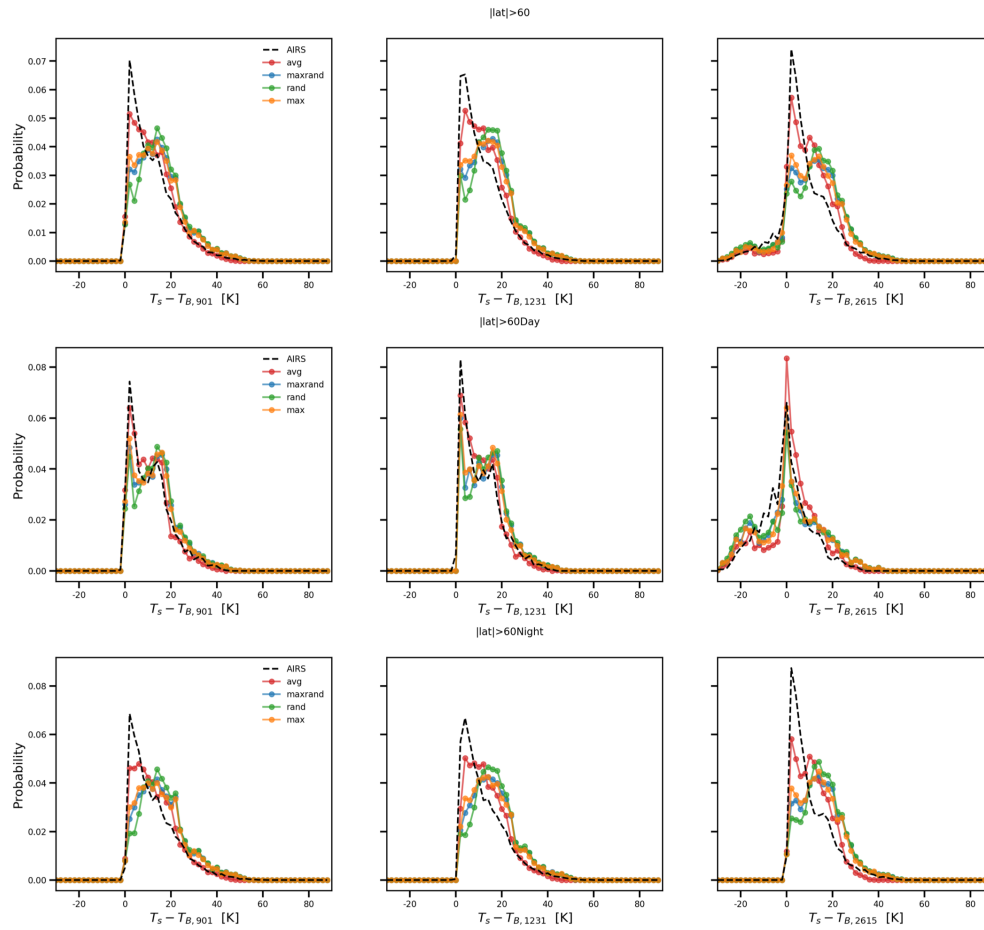


Figure 3.5: Same as Figure 2, but for polar zone only.

3.4 Conclusions and Discussion

In this study, we employ the CRTM models with four different cloud overlap schemes to calculate the TOA radiation field in three atmospheric window channels (both in the thermal and shortwave infrared spectral regions) for a large number of cloudy atmospheric scenarios, and compare the results against AIRS observations using the Wasserstein distance statistical metric. We use 137 vertical levels atmospheric state profiles from ECMWF as the inputs for CRTM. Our results show that CRTM with average overlap scheme successfully predicts the overall probability distribution of clouds over a wide range of spectral channels between 790 cm^{-1} to 1231 cm^{-1} for all 82,271 cases.

CRTM simulations have zone-dependent biases, especially for the polar zone. It has

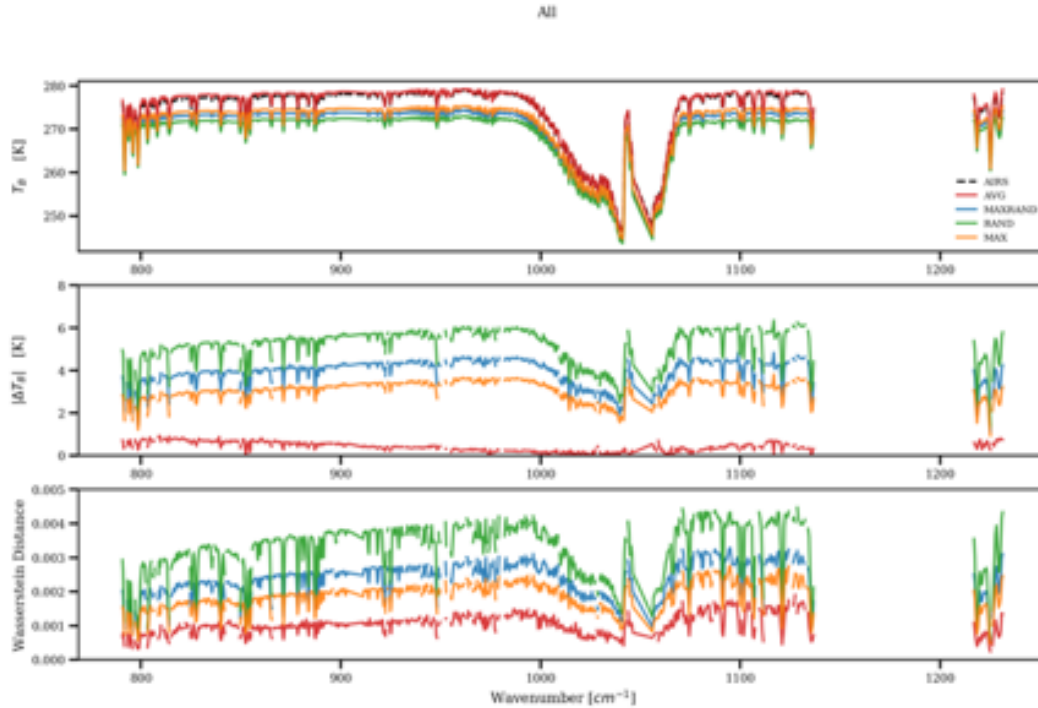


Figure 3.6: (a) Mean brightness temperature, (b) mean absolute difference of brightness temperature, and (c) the first Wasserstein distance between CRTM radiance simulations and all 82,271 AIRS observations for 846 selected AIRS channels between 790 cm^{-1} to 1231 cm^{-1} . The AIRS observations, CRTM with average overlap scheme, maximum-random overlap scheme, random overlap scheme, and maximum overlap scheme results are shown in dashed black, red, blue, green, and orange lines, respectively.

difficulty reproducing the secondary peak of the probability distribution function for the 2615 cm^{-1} channel. Moreover, the pairwise comparison between CRTM average overlap simulations and AIRS radiances shows a regional pattern, there are three possible error sources: (1) random and systematic error from ECMWF cloud profiles (e.g., water/ice cloud content, cloud cover), (2) error due to the oversimplified assumption of cloud overlap scheme, and (3) error from the cloud optical property coefficients. Our approach of comparing the overall probability distribution functions between models and observations can mostly cancel out the random errors in the ECMWF profiles, but not the systematic ones.

Further investigations are required to evaluate the best cloud overlap assumption for different scenarios. One approach could be to use a cloud resolving model (CRM) to create a large number of scenarios with different vertical cloud distributions, with a statistical analysis then performed using the CRM results as the “truth”. It is

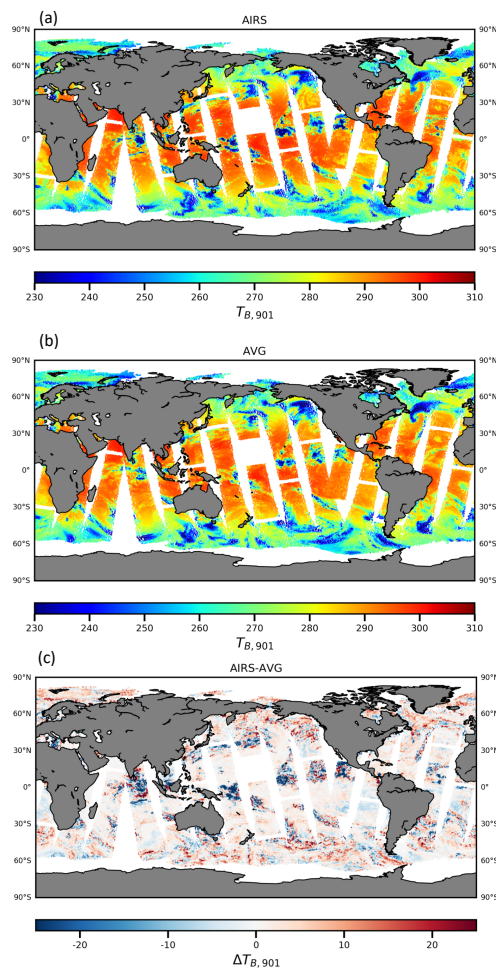


Figure 3.7: Visualization of all 82,271 cases on a global map of 901 cm^{-1} for (a) AIRS observations, (b) CRTM with average overlap scheme, and (c) difference between AIRS observations and CRTM-avg.

also critical to minimize the spatiotemporal mismatch between ECMWF and AIRS locations. Clouds vary a lot in space and time and it is very easy for biases to creep in simply because of errors in characterizing a scene as clear when it is cloudy and vice versa. Finally, the Wasserstein distance is a more superior statistical metric (compared to traditionally used metrics such as the Pearson correlation coefficient) to evaluate the fidelity of RT models with respect to observations, and should be used in future RT model inter-comparisons. The importance of such studies is clearly stated in the recently released Earth Science Decadal Survey (National Academies of Sciences, Engineering, and Medicine, 2018), which recommends a set of observation capabilities that will enable substantial progress in (a) providing critical information on the make-up and distribution of clouds, and (b) addressing

key questions about how changing cloud cover and precipitation will affect climate, weather, and Earth's energy balance in the future.

*Chapter 4*UNDERSTANDING HUMAN IMPACTS ON THE EARTH
SYSTEM

- [1] T. Le, Y. Wang, L. Liu, J. Yang, Y. L. Yung, G. Li, and J. H. Seinfeld. “Unexpected air pollution with marked emission reductions during the COVID-19 outbreak in China”. In: *Science* 369.6504 (2020), pp. 702–706. DOI: 10.1126/science.abb7431.
- [2] Y. Wang, T. Le, G. Chen, Y. L. Yung, H. Su, J. H. Seinfeld, and J. H. Jiang. “Reduced European aerosol emissions suppress winter extremes over northern Eurasia”. In: *Nature Climate Change* 10.3 (2020), pp. 225–230. DOI: 10.1038/s41558-020-0693-4.

4.1 Introduction

The environment on Earth changes constantly, and living systems (including humans) evolve within it for most of history. Since the Industrial Revolution, however, humans have played a dominant role in altering and often destroying the Earth’s environment and living systems in ways never seen before.

Human activities are a series of activities of different scales and types, including agriculture, industry, transportation, and various engineering constructions, which are continuously carried out by humans in order to survive and improve their living standards. Human-made disasters, including pollution and global environmental changes (such as global warming, air pollution, and ozone layer depletion), often lead to environmental degradation, making the environment significantly vulnerable on the one hand, and decreasing the resilience of human beings to disasters on the other. With the effect of these factors, the frequency of natural disasters has grown rapidly as expected.

Greenhouse gases emission is one issue that is of most concern. Starting from the Industrial Revolution, the burning of fossil fuels has been altering the carbon cycle, primarily by increasing CO₂ concentration in the atmosphere. The atmospheric CO₂ concentrations have risen by about 40% compared with pre-industrial revolution levels and are now disrupting the Earth’s climate. Methane (CH₄) is the second most important long-lived greenhouse gas, contributing about 17% of the radiative forcing. About 40% of methane is emitted to the atmosphere through natural

sources (e.g. wetlands and termites), and about 60% of emissions come from human activities such as livestock, rice cultivation, fossil fuel use, landfills, and biomass burning.

Anthropogenic aerosol is another major issue caused by human activities. Aerosols are small particles that exist in the atmosphere in a variety of sizes, concentrations and chemical compositions. Some aerosols are emitted directly into the atmosphere, while others are formed by the reaction of other compounds emitted. Aerosols include both naturally occurring compounds and those formed by anthropogenic emissions. Natural aerosols include mineral dust released from the earth's surface, sea salt aerosols, biological emissions from land and sea, and sulfate and dust aerosols from volcanic eruptions. Anthropogenic emissions include sulfur-containing compounds, organic compounds, and black carbon from the combustion of fossil fuel and biomass and dust from human activities such as open-pit mining and industrial processes. Together with various greenhouse gases, aerosols represent the most significant anthropogenic forcing responsible for climate change. On one hand, the absorbing aerosols such as black carbon can reduce the effective albedo and increase solar forcing over clouds and snow. On the other hand, non-absorbing aerosols such as sulfate can enhance the effective albedo and reduce solar forcing over dark surfaces. Also, aerosols can affect the cloud number density and cloud droplet size indirectly, and thereby affect cloud radiative forcing.

Practically speaking, aerosols are linked to air quality, visibility, and human health. Aerosols limit visibility and cause haze in the cities. In addition, aerosols inhaled by people can damage lung tissue and cause lung disease. Therefore, understanding the aerosol's impact on the Earth's system and designing the emission control plans are critically important for society.

In this chapter, we work on two more realistic problems than what we were dealing with in the previous chapters. In Section 4.2, we study the relationship between radiative forcing due to anthropogenic aerosols and winter extreme weather in the Northern Hemisphere during 1970-2005, which is a unique transition period for global aerosol forcing. In Section 4.3, we review hyperspectral satellite and ground-based observations and conduct state-of-art atmospheric model simulations during the COVID-19 lockdown period.

4.2 Signature of Anthropogenic Aerosols on Winter Extreme Weather

4.2.1 Introduction

Wintertime extreme cold temperature, frost, and blizzard impact billions of people living in the mid-latitude regions, especially the populous Northern Hemisphere (NH). However, an understanding the decadal and interdecadal trends of winter extreme events remains elusive, as studies based on data from different sources (reanalysis, surface stations, etc.) over varying time periods show large disparity in trend assessments [86, 87, 88]. More fundamentally, the lack of consensus on changes of winter extreme weather stems from the intrinsic complexity of the physical basis for mid-latitude weather systems as well as the rapidly changing environmental factors causing the winter extremes. From the climate perspective, a significant portion of the complexity can be attributed to the tangled natural variabilities in the Earth system, such as the Northern Annular Mode (NAM) [89]. The role of anthropogenic forcing in winter extremes is also highly uncertain, as the dynamical responses tend to be multifaceted and nonlinear. For example, a warming climate characterized by polar amplification is believed to reduce the meridional temperature gradient and result in a slower, but more complex mid-latitude jet stream that steers synoptic cyclones and blocking anticyclones [90, 91]. On the other hand, air advected from the polar region to the mid-latitudes can become less cold as a result of a warmer Arctic, reducing the possibility of extreme cold temperatures [92]. Moreover, the tropical expansion of the Hadley cell in response to global warming can move the jet streams pole-ward and counteract the influence of Arctic sea ice loss [93], forming a “tug-of-war” paradigm [94].

As the second largest climate forcer in the Earth system, atmospheric aerosols have been linked to climatic changes in both mean state and extreme events via their effects on radiation fluxes as well as cloud microphysics [95, 96, 97]. The global distribution of anthropogenic aerosols (AA) is highly heterogeneous spatially, and, more importantly, anthropogenic emission sources have changed notably and distinctively over different regions on the decadal time scale. Since the 1970s, the global focus of aerosol emissions has migrated from the developed countries in Europe and North America to the developing countries like China and India [98]. Consequently, an overall positive radiative forcing has emerged out of the reduction in AA in Europe and North America, along with a strong negative forcing in China and India. Such a “see-saw” radiative forcing pattern was further found to regulate the large-scale circulation, alter the hydrological cycle, and even have the potential of interfering with the pace of Arctic sea ice melting [99].

The extent to which such a characteristic AA forcing pattern shift modulates extreme weather events by changing the dynamics of circulation systems and mid-latitude Rossby waves has not been investigated. Therefore, the present study aims to unravel the historical impacts of anthropogenic aerosol forcing on weather-scale atmospheric circulation systems and winter extremes by examining long-term reanalysis data and conducting numerical simulations using a state-of-the-art global climate model. To assess precisely the impacts of the anthropogenic emission shift, we confine our analysis period to 1970-2005, during which the geospatial contrast of AA trends was the largest and occurred contemporaneously with greenhouse gas accumulation.

4.2.2 Methods and data

4.2.2.1 Local Wave Activity (LWA)

LWA is used to characterize the midlatitude extreme weather events by jointly considering their frequency as well as intensity [100]. It captures the meridional eddy fluxes that produce meridional areal displacement of geopotential height (z) isopleth at 500 hPa ($Z500$):

$$LWA(\lambda, \phi_e) \equiv \frac{a}{\cos \phi_e} \left(\left| \int_{\hat{z} \leq 0, \phi \leq \phi_e(z), \lambda = const} \hat{z} \cos \phi d\phi \right| + \left| \int_{\hat{z} \geq 0, \phi \geq \phi_e(z), \lambda = const} \hat{z} \cos \phi d\phi \right| \right) \quad (4.1)$$

where λ is longitude, ϕ is latitude, a is the radius of Earth, $\hat{z} = z - \bar{Z}$ is the eddy of geopotential height, and ϕ_e is the equivalent latitude bounding the same area toward the North Pole as of that by a certain z isopleth. We calculate LWA based on 6-hour data.

4.2.2.2 Jet Stream Sinuosity Analysis

The transient sinuosity of the meandering jet stream provides a direct description of the ongoing weather systems in mid-latitudes. The slower but wavier jet stream is generally accompanied by more extreme weather systems, such as low/high pressure and strong frontal systems. The sinuosity of the jet stream is typically defined as the ratio between the length of a trajectory and the length of the shortest straight line between two points. We derive the transient sinuosity of the jet stream (abbreviated as sinuosity hereafter) based on the 6-hourly geopotential height at 500 hPa from the reanalysis data. We first calculate $Z500$ mean value (\bar{Z}) for a mean latitude ($\bar{\phi}$) over a certain latitude zone in NH (20-80° in this study), and then find the contour

line of Z in the 2-D map of $Z500$. The sinuosity is the ratio between the length of the contour line and the length of the latitude circle for $\bar{\phi}$. Such an index was developed to study the jet stream response to global warming [101].

4.2.2.3 Removing Natural Variability by Multi-linear Regression

We apply a multivariate linear regression model to extract the anthropogenic influence from natural impacts on the winter extreme weather. The model has a form:

$$LWA = a \cdot AO + b \cdot PDO + c \cdot Strato + d \cdot ENSO + e \cdot QBO + residuals \quad (4.2)$$

where $a - e$ are regression coefficients. The LWA values going into the regression are the winter means at each grid point in NH. Five climate indices are considered here, including the Arctic Oscillation (AO), Pacific Decadal Oscillation (PDO), stratosphere variability (Strato), El Niño–Southern Oscillation (ENSO) and Quasi-Biennial Oscillation (QBO). They are calculated over the boreal winter (December to February) of each year as well. Rossby wave activity can be influenced by stratospheric variability (for example, ref [102]), especially in the winter when the stratospheric polar vortex is strong. Hence, we derive an index (Strato) using the monthly mean zonal wind at 10 hPa and 60° N to account for such stratospheric variability.

4.2.2.4 Reanalysis Data

6-hourly geopotential height and surface temperature data during 1970-2005 are used from the Japanese 55-year Reanalysis (JRA55)[103] which is one of very few datasets tracing back beyond 1979.

4.2.2.5 Global Aerosol-Climate Model Simulations

The National Center for Atmospheric Research–Department of Energy CESM (version 1.2.2)—an updated version of CESM 1.0 participating in the Coupled Model Intercomparison Project Phase 5—is used in this study to simulate the historical variations of winter extreme weather and to conduct attribution analyses. The atmospheric circulation model (Community Atmosphere Model 5.4) fully interacts with an ocean circulation model (Parallel Ocean Program 2), a sea ice model (CICE) and a land-surface model (Community Land Model) through a central coupler. The model is 1° horizontal resolution in both atmosphere and ocean models. Six types of

aerosols (sulfate, black carbon, primary organic matter, secondary organic aerosol, sea salt and dust) are considered in the three-mode version of Modal Aerosol Module 3. The aerosol interactions with atmospheric radiation fluxes, aerosol–cloud interaction (grid-scale stratiform clouds) and the effect of absorbing aerosols (black carbon and dust) deposited in the snowpack are explicitly considered in the physics of CESM 1. More details regarding the treatments of aerosol, clouds and convection in CESM 1 can be found in our previous work [99].

To precisely assess the impacts of the anthropogenic emission shift, we confined our analysis period to 1970–2005, during which time the geospatial contrast of anthropogenic aerosol trends was the largest and occurred contemporaneously with greenhouse gas emissions. To minimize the spread of internal model variability from transient radiative forcing before 1970, one historical simulation was first created from 1850–1970, and then ensemble sensitivity simulations branched out for another 36-year integration. Two emissions scenarios were considered during 1970–2005: ALL and NO_AERO. Considering the significant nonlinearity in certain climate responses to different external forcings [104, 105, 106], such as the wave activity in the present study, the differences between those two experiments can only be interpreted as the qualitative importance of aerosol effects for those results. We prefer this method to aerosol only simulations that ignore all other forcings and deviate from the real climate state. Accounting for the dependence of aerosol forcing on all other forcings is especially important in the transient forcing experiments that aim to mimic the real world.

4.2.3 Results

To examine variations of winter extreme events at each individual region, we employ here the local Rossby-wave activity (LWA) index. LWA has been developed and used to quantify the frequency and intensity of synoptic weather systems influencing individual locations in mid-latitudes [100]. A larger LWA indicates more severe weather events, either extratropical cyclone or blocking anticyclone. The observed long-term wintertime LWA trends are derived based on the 500 hPa geopotential height from reanalysis.

A spatial map of LWA trends during 1970–2005 (Figure 4.1(a)) shows the existence of geospatial variations of winter weather systems behind an overall declining LWA trend. The major reductions in LWA occurred in the northern part of the Eurasian continent and Eastern Canada, with varying statistical significance in the trends.

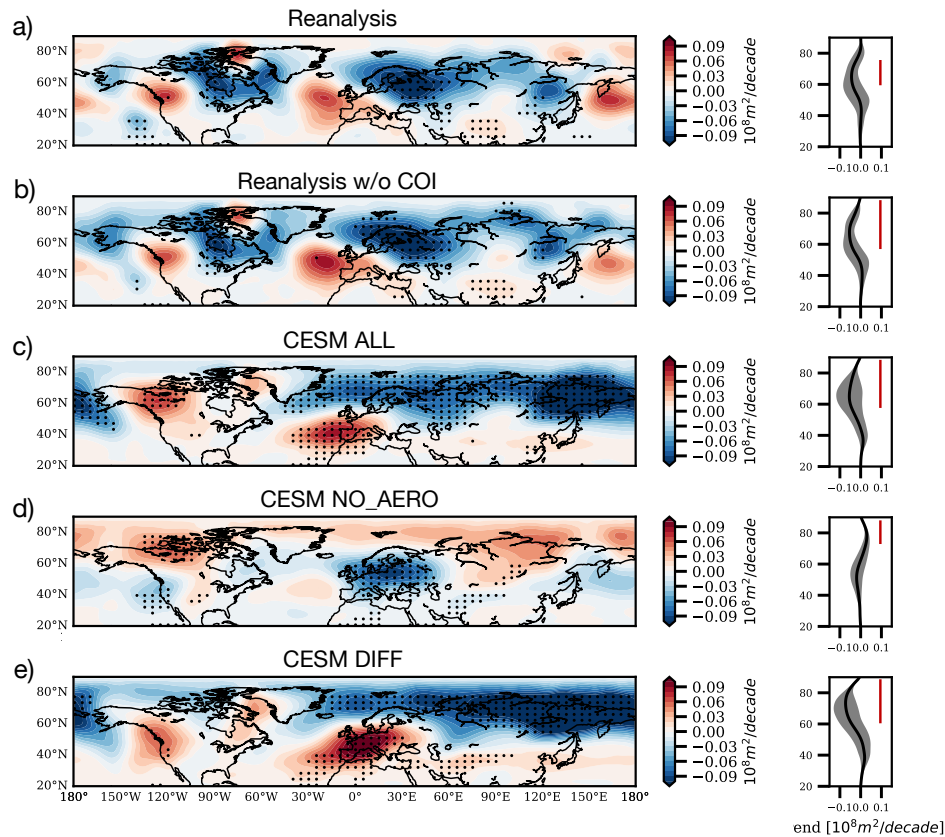


Figure 4.1: CLWA trends from reanalysis and model simulation over December to February during 1970–2005. a–e, Spatial patterns of LWA trends (left column) and their zonal mean distribution (right column) for: JRA55 (a); JRA55 with removal of trends in major known climate oscillation indices (b); CESM ALL results (c); CESM NO_AERO results (d); and CESM ALL – NO_AERO (DIFF) (e). Black dots (each representing 16 grid points) indicate that the local linear trend is significant at the 90 % confidence level using a Student's t-test. Shading in the zonal mean plots indicates spread of the LWA trend at the same latitude. The red vertical bars denote latitude zones with significant LWA trends (shades do not overlap with the 0 m² per decade line).

Western Europe, Western Canada, and the Northwest Pacific are the regions where synoptic weather systems became more frequent from 1970 to 2005, however, all of those increasing trends are insignificant at the 95% significance level. When we further decompose the LWA into cyclone and anticyclone events, it is found that the LWA trends near the western coasts of the Eurasia and North America continents are all related with cyclones, while those near the eastern coasts are caused by anticyclones (Figure 4.2). Those agree with the climatological locations of the NH winter cyclone/anticyclone.

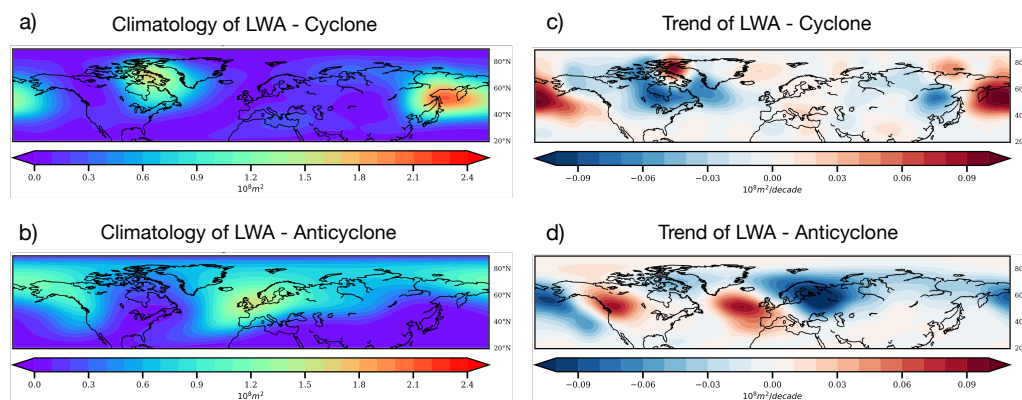


Figure 4.2: Climatology and trends (1970-2005) of cyclonic and anticyclonic wave activities based on JRA-55.

The zonal means of LWA trends show no significant trend over the latitude bands south of 50°N . The most prominent change in LWA occurred near 65°N with the largest declining trend. Similar with the sinuosity of the jet stream, NH mean of LWA shows an insignificant negative trend during 1970-2005 (Figure 4.3). Considering that in this period, significant global warming with about $+0.12^{\circ}\text{C}$ per decade surface temperature increase occurred, the existing theory that enhanced jet stream sinuosity and LWA follow the polar amplification is not capable of explaining such an interdecadal trend. There must be other factors at play.

To better characterize the variation of extreme weather, we also examine the top 10% in wave amplitude of LWA during each season and their trends (Figure 4.4). The spatial patterns of the extreme LWA trends resemble well with the seasonal mean LWA trends, showing a consistent and significant reduction over Northern Eurasia.

By individually correlating the time series of seasonal Northern Hemisphere mean LWA with six climate oscillation indices, we are able to identify those that ex-

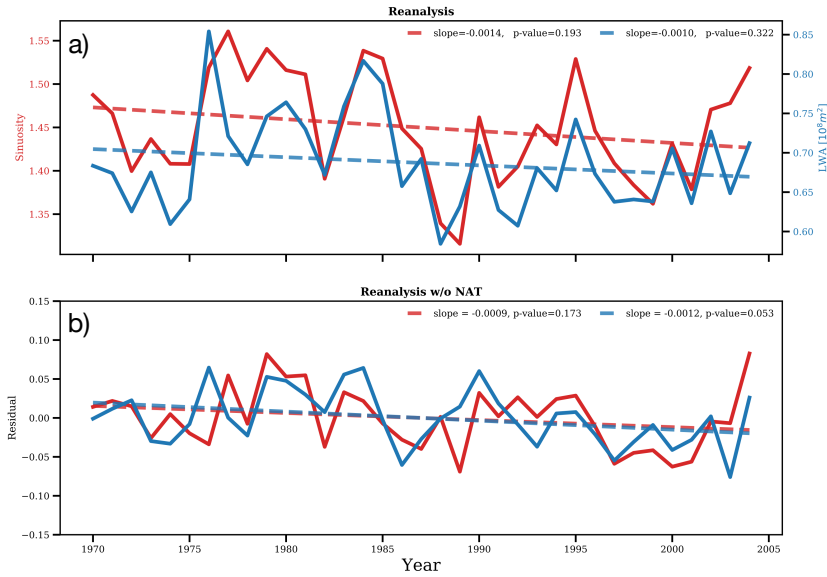


Figure 4.3: Northern Hemispheric trends of jet stream sinuosity and local wave activity (LWA) during 1970-2005 based on JRA55 Reanalysis. The bottom panel shows the results with removal of natural variability (NAT) by the multivariate linear regression method.

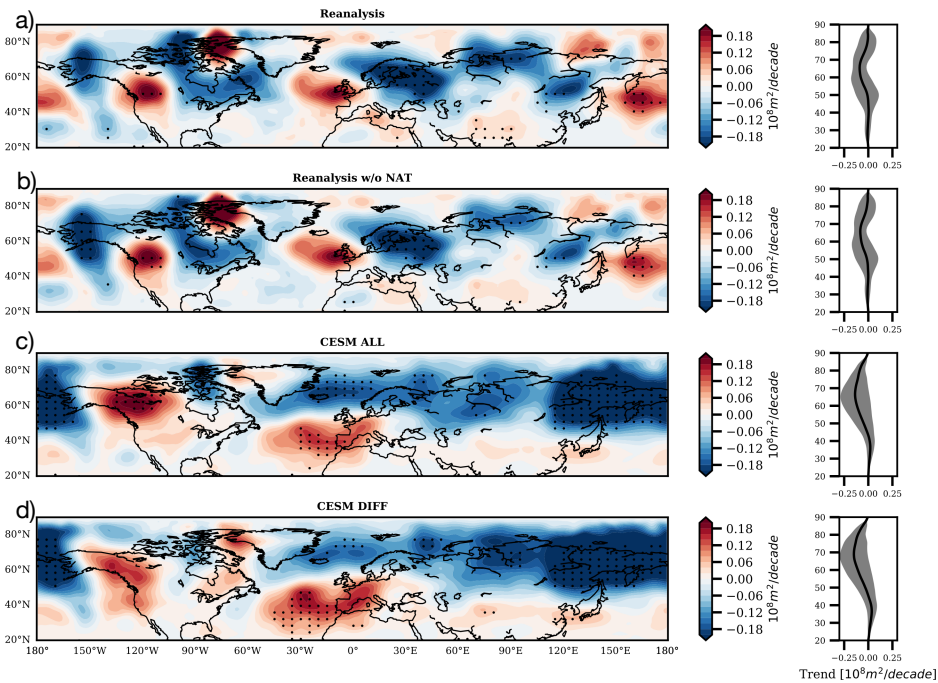


Figure 4.4: Same with Figure 1 but for top 10% LWA during each season. They indicate the extreme LWA cases and strongest cyclonic/anticyclonic events.

plain the weather extreme variability on the interannual time scale. The Arctic Oscillation (AO, or NAM) and the North Atlantic Oscillation (NAO) are the two most pronounced climate variabilities exhibiting close relationships with LWA over Northern Hemisphere mid-latitudes, with correlation coefficients about -0.83 and -0.66, respectively. The anti-correlations agree with previous studies that analyzed those relationships in different time periods⁴. The PDO exhibits a much weaker correlation with LWA, with a coefficient of +0.33. The Stratospheric variability (Strato.), El Niño- Southern Oscillation (ENSO), and Quasi-Biennial Oscillation (QBO) play even smaller roles in the year-to-year variability of LWA, with the coefficients < 0.1 . To extract the possible influence of the natural variabilities on the decadal trend detected above, we performed a multivariate linear regression of LWA on those five natural variability indices. The trends in the residues after the regression better reflect the anthropogenic influence on the weather variability. By removing the natural variability over each location of NH, the overall spatial distribution of LWA trends still hold, even with increases in the statistical significance over Northern Eurasia and northern Atlantic (Figure 1b). Similarly, the declining trends of LWA extremes over Northern Eurasia remain robust after removing the possible influence from the natural variabilities (Figure 4.4). These results corroborate the assertion that anthropogenic influence is critical in regulating the Rossby waves over NH mid-latitudes during the wintertime from 1970 to 2005. Moreover, the trends based on the reanalysis data remain robust even with an analysis period starting from 1979, the beginning of the satellite era.

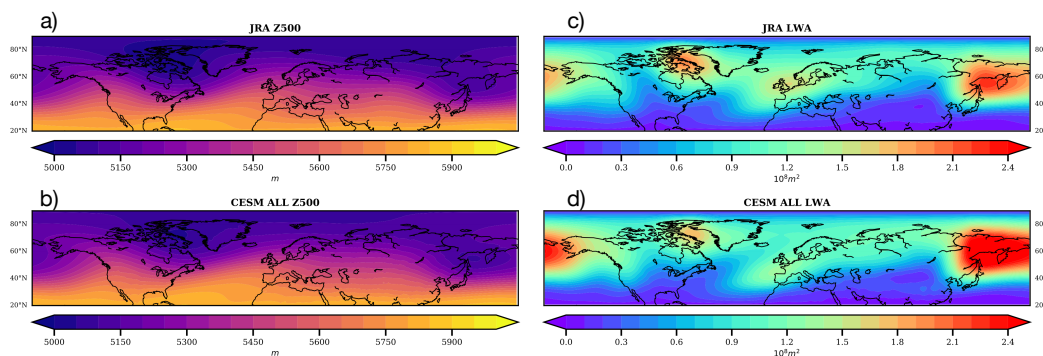


Figure 4.5: Comparison of climatological geopotential height at 500 hPa (Z500) and local wave activity (LWA) between JRA-55 and the CESM all forcing experiment.

To further attribute the observed trends of LWA, we perform transient-forcing sensitivity simulations using a fully coupled global climate model with comprehensive representations of radiative forcings in the Earth system. Ensemble climate simulations were conducted by the NCAR/DOE Community Earth System Model (CESM) Version 1.2.2, which simulates reliable climatology of geopotential height and LWA (Figure 4.5). To simulate the AA shift since the 1970s, two groups of ensemble simulations were performed with and without transient variations of AA emissions from 1970 to 2005. The differences between those two groups emerge as aerosol impacts (hereafter denoted as AERO). All-forcing CESM simulations (hereafter denoted as ALL) show quite similar trends of winter LWA in NH by reproducing the most significant LWA decreasing region over Northern Eurasia as well as increasing regions like Western Europe and Western Canada (Figure 4.1(c)). Such a consistency supports the fidelity of CESM in reproducing the past climate and justifies use of such a model in the attribution analysis. Nevertheless, some model discrepancy exists in the trends of LWA over the Northwest Pacific and Eastern Canada, even though those trends are not statistically significant in the reanalysis data. Note that a previous study¹⁰ suggested that the intensified Pacific storm track as a result of Asian pollution outflow cannot be reproduced in a conventional global climate model in which the convective parameterizations do not include the aerosol effect on cloud microphysics for deep convective clouds. More importantly, the spatial patterns in AERO largely resemble those in ALL (Figure 4.1(e)), as both show a reduction of winter extremes in Northern Eurasia and increases in Western Europe and western coasts of US and Canada. The resemblance of LWA trend patterns among reanalysis, ALL, and AERO indicates the AA historical variations as a dominant factor to explain the changes in winter extreme events over Eurasia from 1970 to 2005.

4.2.4 Conclusion

In contrast to previous studies on aerosol effects on the mean state changes in climate and circulation, the present study focuses on a unique period of transient aerosol forcing on the weather extremes and the resulting decadal trends. By combining long-term observational data and a state-of-the-art climate model, the unambiguous signature of anthropogenic aerosols on the wintertime jet stream and Rossby waves on the interdecadal time scale is confirmed, which alters day-to-day surface temperature variability. Compared with previous studies focusing on greenhouse gas forcing and its consequence on Arctic amplification [91, 92, 94, 107, 108, 90], the

current study provides a new perspective on spatially inhomogeneous aerosol forcing when explaining the trends of winter weather extreme events. The magnitude of future anthropogenic aerosol reduction in Europe and US is not anticipated to be the same as that in 1970-2005. Moreover, Asian aerosol levels are projected to decrease in the next few decades. The anticipated pattern of aerosol forcing will result in different perturbations on the jet stream and LWA. To what extent future aerosol changes will be distinguished from the ever-growing greenhouse gas concentration is still an open question. It has been suggested that future NH aerosol reductions will be linked to a slowdown of the increase in summer extreme weather[109]. The accuracy of this present detection and attribution study draw upon the robustness of the unique JRA55 reanalysis dataset.

4.2.5 Appendix

4.2.5.1 Recipe for the calculation of local wave activity

We illustrate the calculation of LWA using the weather map on 1200 UTC 13 Feb 1983. The calculation is performed for the latitudes of 20N-90N. The detailed calculation procedure is listed below.

- 1 Choose a latitude of interest, ϕ . Use 50 N for example.
- 2 Determine the corresponding Z500 contour such that the equivalent latitude of the contour satisfies $\phi_e = \phi$ equivalent latitude is obtained from the area from the Z500 contour to the North Pole via box counting and converting the area to a hypothetical equivalent latitude such that the contour is zonally symmetric. Figure 4.6(a) gives the Z500 contour (solid red) with the equivalent latitude of 50N (dashed red).
- 3 Compute the eddy term $\hat{z} = z - Z500$ or the calculation at each latitude, only the values between the latitude ϕ and contour Z500 will be used. See Figure 4.6(b). Note that z is the actual geopotential height, and \hat{z} is the difference between the actual geopotential height and the Z500 for the equivalent latitude.
- 4 The line integral for the southern cyclonic LWA is computed at the longitude λ by box-counting \hat{z} in the southern grid boxes relative to the latitude ϕ_e that satisfy $\hat{z} \leq 0$. Similarly, the northern anticyclonic LWA is calculated for the northern grid boxes satisfying $\hat{z} \geq 0$. LWA at $\phi = 50N$ is shown in Figure 4.6(c). This is compared with the product of the zonal amplitude \hat{z} and meridional amplitude $\hat{\phi}$

of a planetary wave described in [110], where \hat{z} is the deviation of the geopotential height from the zonal mean, and $\hat{\phi}$ is the meridional displacement of the contour. In the small amplitude limit, $LWA = -0.5a\hat{z}\hat{\phi}$ ([100]), where a is Earth's radius.

5 Repeat steps 1-4 for all the other latitudes. The longitude by latitude map of LWA is shown in Figure 4.6(d).

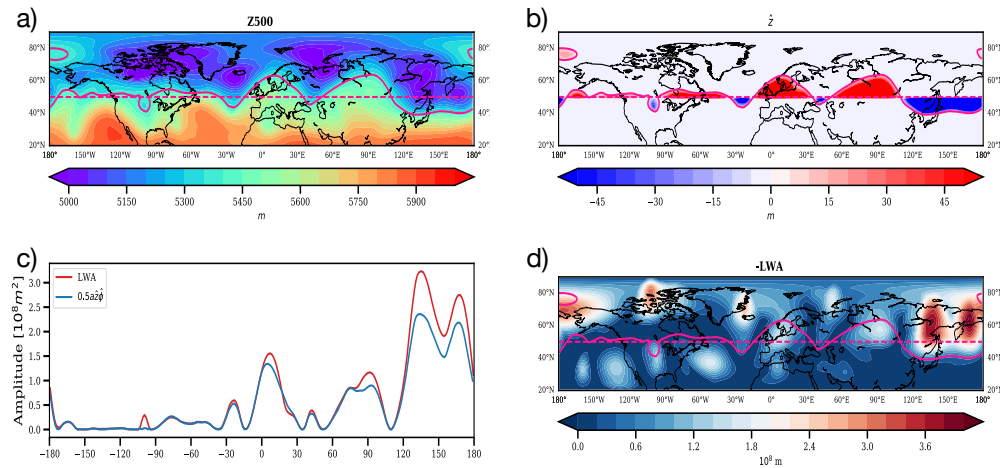


Figure 4.6: (a) Z500 as a function of longitude and latitude. (b) The eddy term \hat{z} plotted between the latitude 50N and the contour with the equivalent latitude $\phi_e = 50N$. (c) LWA at 50N as a function of longitude (red). The product of the zonal amplitude \hat{z} and meridional amplitude $\hat{\phi}$ of a planetary wave (blue). In the small amplitude limit, $LWA = -0.5a\hat{z}\hat{\phi}$ (d) -LWA as a function of longitude and latitude. In (a), (b) and (d), the contour with the equivalent latitude $\phi_e = 50N$ shown in solid red, and the latitude 50N is in dashed red.

4.3 Unexpected air pollution with marked emission reductions during the COVID-19 outbreak in China

4.3.1 Introduction

The abrupt outbreak of the Corona Virus Disease 2019 (COVID-19) pandemic produced unprecedented societal impacts in China. To curb the virus spread among humans, a preventive lockdown was first implemented on January 23rd in Wuhan, Hubei. Other major cities/counties in China subsequently followed suit, and the entire nation's lockdown lasted for at least three weeks (varying in different regions). During the lockdown period, emissions from the traffic sector were drastically reduced. Such a shutdown serves as a natural experiment to evaluate air quality responses to a dramatic emissions reduction and to assess the interplay between emission, atmospheric chemistry, and meteorological conditions. Here, we synthesize multiple-year satellite retrieved atmospheric compositions, national ground station measurements of major pollutants, meteorology from reanalysis data, and a suite of state-of-the-art online atmospheric chemistry model simulations to assess the atmospheric influence of the COVID-19 outbreak in China and to reveal its implications for air pollution control strategies.

China has continued to battle particulate haze pollution [111]. Long-term regulatory plans targeting energy and industrial emissions have been implemented [112], and nation-wide improvement of fine particulate matter levels has been reported [113]. Nonetheless, the key chemical and physical processes responsible for severe haze formation in China remain elusive, including exacerbated ozone levels [114, 115], pathways of secondary aerosol formation [116, 117], and emissions-meteorology interactions [118]. Certain societal events in China with short-term stringent emission controls have been studied as natural experiments, such as the "Olympic Blue" during the 2008 Beijing Summer Olympic Games [119] and the "APEC Blue" during the 2014 Asia-Pacific Economic Cooperation (APEC) Economic Leaders' Meetings in Beijing [120, 121]. Emission controls during these two events resulted in 40-60% reduction in SO₂, NO₂, non-methane volatile organic compounds (VOCs), and particulate matter.

4.3.2 Methods and data

4.3.2.1 Satellite product

The TROPOMI instrument onboard the Copernicus Sentinel-5P satellite provides daily global coverage of tropospheric column density of NO₂ with a spatial resolution

$3.5 \times 7 \text{ km}^2$ ($3.5 \times 5.5 \text{ km}^2$ starting from August 6, 2019) with overpass time around 13:30. The TROPOMI NO₂ processing system is based on the algorithm developments for the DOMINO-2 product and for the EU QA4ECV NO₂ reprocessed dataset for OMI, and has been adapted for TROPOMI. In this study, the tropospheric NO₂ column densities were taken from S-5P/TROPOMI Level 2 offline products. The measurements with a Quality Assurance (QA) value less than 0.5 were omitted, which removed the measurements with processing errors, anomalously high signals, and sun glints. We re-gridded the Level 2 product on a $0.03^\circ \times 0.03^\circ$ spatial grid which corresponds to 3.3 km in latitude.

The MODIS Level 3 AOD datasets are from Aqua and Terra with $1^\circ \times 1^\circ$ spatial resolution. We generate the Level 3 daily map by using the average value of Aqua and Terra measurements.

4.3.2.2 Ground station observations

Hourly air quality data have been obtained from the national urban air quality real-time platform released by the China National Environmental Monitoring Station (website: <http://106.37.208.233:20035>). The method of measuring air quality follows the national standard of GB 3095-2012. Measurement of PM_{2.5} was carried out by the β Ray absorption method and micro-oscillation balance method; measurement of NO₂ is by the Chemiluminescence method; measurement of SO₂ and O₃ is by the UV fluorescence method; measurement of CO is by the non-dispersive infrared absorption method and gas filter correlation infrared absorption method. Monitoring stations usually avoid tall buildings, trees and other potential obstacles that would impede air circulation. The surroundings of air monitoring site have been guaranteed with stable electricity supplies and device maintenance service. Sampling ports are 3 to 15 meters above the ground. The distance between each sampling port exceeds 1 m. Temperature inside the monitoring stations is maintained between 15 and 35°C, relative humidity $\leq 85\%$, and atmospheric pressure between 80 and 106 kPa.

4.3.2.3 Reanalysis data

The boundary layer height, precipitation, relative humidity at 1000 hPa and the wind vector $w = (u, v)$ at 10 meters above the ground were taken from the ERA5 reanalysis data with $0.25^\circ \times 0.25^\circ$ spatial resolution. ERA5 combines historical

observations into global estimates using advanced modelling and data assimilation systems.

4.3.2.4 WRF-Chem model simulations

The model used in this study is based on a specific version of the WRF-Chem model [122] with modification by [123, 124, 125, 126]. The specific WRF-Chem model includes a flexible gas phase chemical module with consideration of different chemical mechanisms and the CMAQ aerosol module (AERO5) developed by US EPA [127]. The organic aerosols (OA) are simulated using the volatility basis-set (VBS) modeling method, with the secondary OA (SOA) contributions from glyoxal and methylglyoxal. ISORROPIA (Version 1.7) is used to predict the inorganic aerosols, calculating the composition and phase state of an ammonium-sulfate-nitrate-water inorganic aerosol in thermodynamic equilibrium with gas phase precursors [128]. Three major types of heterogeneous aerosol chemistry are considered: the heterogeneous hydrolysis of N_2O_5 on the surface of deliquescent aerosols to form nitrate, the heterogeneous reaction of SO_2 involving aerosol water to form sulfate, and the heterogeneous reaction of glyoxal and methylglyoxal to form SOA. The anthropogenic

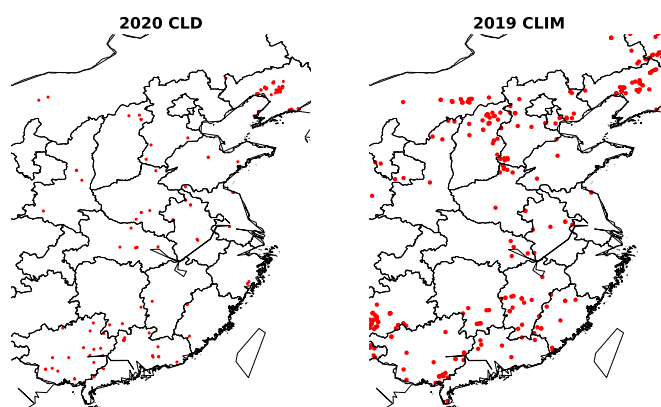


Figure 4.7: Accumulated fire counts based on MODIS Active Fire Products over three-week periods during 2020-CLD and 2019-CLIM. Fire counts can be used to indicate the biomass burning in the agricultural activities. Dots in the plots are with confidence level larger than 80 in the MODIS product.

emission inventory is developed by [129] with the base year of 2020, including industry, transportation, power plant, residential and agriculture sources. The Model of Emissions of Gases and Aerosols from Nature (MEGAN) is used to calculate the biogenic emissions online [130]. Biomass burning emissions are potentially important for Asian haze [131, 132, 133, 134]. Fire counts from satellites can partly

reflect BB in agricultural activities and wildfires. In the Figure 4.7, we analyzed the MODIS fire counts during the 2020 city-lockdown period and found very few fire activities in the Beijing-Tianjin-Hebei area. Moreover, the fires were more frequent in the same period of 2019 than that in 2020 over the whole nation. Therefore, we conclude that BB from agriculture and wildfires did not contribute significantly to the haze formation during the 2020-CLD, and we did not consider them in our WRF-Chem simulations. A haze episode from 21 January to 16 February 2020 in the North China Plain is simulated using the WRF-Chem model, and detailed model configuration can be found in Table 4.1. A series of model sensitivity experiments are conducted, and the experiment descriptions are provided in Table 4.2.

Region	East Asia
Simulation period	2020-01-21 to 2020-02-16
Domain size	400 × 400
Domain center	35.0°N, 114.0°E
Horizontal resolution	12km × 12km
Vertical resolution	35 vertical levels with a stretched vertical grid with spacing ranging from 30m near the surface, to 500m at 2.5km and 1km above 14km
Microphysics scheme	WSM 6-class graupel scheme [135]
Boundary layer scheme	MYJ TKE scheme [136]
Surface layer scheme	MYJ surface scheme [136]
Land-surface scheme	Unified Noah land-surface model [137]
Long-wave radiation scheme	Goddard longwave scheme [138]
Short-wave radiation scheme	Goddard shortwave scheme [139]
Meteorological boundary and initial conditions	NCEP 1°×1° reanalysis data
Chemical initial and boundary conditions	MOZART 6-hour output [140]
Anthropogenic emission inventory	SAPRC-99 chemical mechanism emissions [129]
Biogenic emission inventory	MEGAN model developed by [130]
Model spin-up time	24 hours

Table 4.1: WRF-Chem model configurations.

Experiments	Configuration	Purpose
Baseline	Described in Table 4.1.	To reproduce observed pollution changes.
Clim_Met	Using Climatological meteorological initial and boundary conditions averaged over the same time periods during 2015 - 2019.	To assess the meteorological influence on pollution changes.
NO _x _80	According to the satellite observations, increasing NO _x emissions in all sectors by 80% from the baseline simulation to reflect the non-COVID19 scenario.	To assess effect of NO _x reduction.
Heteoro_Chem	Turning off all heterogeneous chemistry processes in our modified version of WRF-Chem.	To assess the contribution of heterogeneous chemistry to the haze formation.
VOC	Increasing/Decreasing VOC emissions by 30%.	To assess the sensitivity of VOC emissions to the haze formation.

Table 4.2: Model sensitivity experiment description.

4.3.3 Results

The primary focus period during the COVID-19 lockdown in China was from January 23 to February 13, 2020 (hereafter referred to as the 2020-CLD period). This period encompassed a 7-day national holiday traditionally celebrating the Lunar New Year, during which previous studies have noted the reduction in anthropogenic emissions [141]. Nitrogen dioxide (NO₂) is key in atmospheric chemistry and serves as an important precursor for both ozone production and secondary aerosol formation [116, 142]. Changes in NO₂ during the lockdown period can be assessed by comparing spaceborne NO₂ measurements in the same time periods over different years. The TROPospheric Monitoring Instrument (TROPOMI) on board the Copernicus Sentinel-5 Precursor satellite has provided key trace gas measurements of high accuracy since 2018. TROPOMI data show quite low column-integrated NO₂ amount during the 2020-CLD, with a mean value of 1.72 mg m⁻², and general uniformity throughout the whole country (Figure 4.8(A)). By contrast, in the same period in 2019, hot spots of NO₂ were evident over eastern China, where the re-

gional mean NO_2 abundance was 4-5 times higher than that in other regions of China (Figure 4.8(B)). Regional means over eastern China experienced a $5.70 \text{ mg} \cdot \text{m}^{-2}$ reduction in NO_2 , corresponding to a -71.9% fractional change (Figure 4.8(C)). At the peak of the disease outbreak, Wuhan experienced a 93% fractional reduction in NO_2 . Such a short-term human-induced reduction in NO_2 is unprecedented, well exceeding the previous 2014 “APEC-Blue” with largest NO_2 reduction of about 40% (10). Compared to a five-year climatology (2015-2019) based on the NASA Aura Ozone Monitoring Instrument (OMI), the NO_2 reductions mainly occurred over the North China Plain.

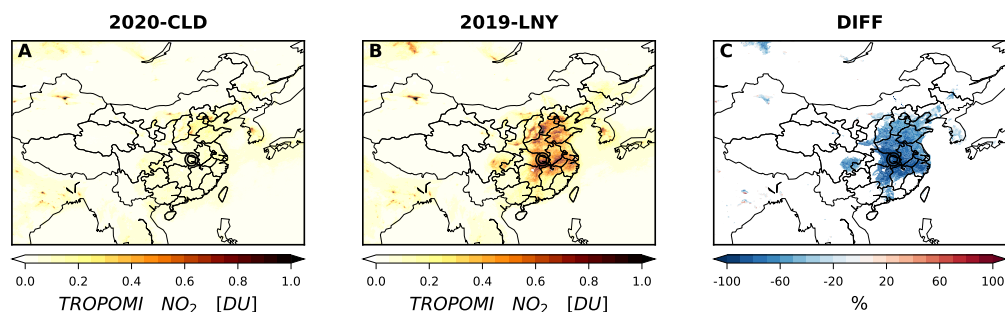


Figure 4.8: Spaceborne measurements of NO_2 from TROPOMI. (A) Column-integrated NO_2 averaged over the COVID19 lockdown period (CLD) for three weeks during Jan. 23 to Feb. 13, 2020. (B) Column-integrated NO_2 averaged over the reference period in 2019. To account for the annual holiday, the 2019 reference period we choose is the same as that in 2020-CLD in the Chinese lunar calendar, starting from the two days before the Chinese Lunar New Year (2019-LNY). Note that TROPOMI NO_2 is available only starting from June 2018. (C) The fractional changes between (A) and (B), calculated only for the regions with NO_2 in 2019-LNY greater than 0.2 DU. The symbols in the maps indicate the location of Wuhan, the most affected city by the COVID-19 disease. 1 Dobson Unit (DU) = $0.4462 \text{ mmol m}^{-2}$.

In addition to spaceborne retrievals, we explore surface measurements of fine-mode aerosols and trace gas species over entire eastern China. We calculate separately the climatological means of the past five years (2015-2019) during the same three-week period as the CLD, including the Lunar New Year (hereafter referred to as CLIM-LNY) and the same three-week period in the Georgian Calendar (CLIM). The difference between CLIM-LNY and CLIM is attributed mainly to the holiday effect. In Wuhan, surface concentrations of NO_2 and SO_2 were the lowest compared with the three-week means before the CLD as well as the climatological means over the past five years. $\text{PM}_{2.5}$ (particulate matter with aerodynamic diameter less than 2.5

μm) was reduced by $23.2 \mu\text{gm}^{-3}$ (-32.4%) and $37.4 \mu\text{gm}^{-3}$ (-43.5%) as compared to CLIM-LNY and CLIM, respectively (Figure 4.9(A)). In contrast to the changes to the PM_{2.5}, surface ozone mixing ratio showed a +5.0 ppb (+25.1%) enhancement in Wuhan during the CLD as compared to CLIM-LNY. Ozone chemistry is highly nonlinear, and in the wintertime urban areas in China, its production is in a NO_x-saturated regime (NO_x = NO + NO₂) due to the relative lack of HO_x radicals [142]. Besides, reduction of fresh NO emissions alleviates ozone titration [142, 143]. Thus, a reduction of NO_x leads to an increase in ozone. Previous studies also attributed the anticorrelation between PM_{2.5} and ozone to the aerosol radiative effect on the photochemistry of ozone formation [114, 144] as well as the aerosol sink for ozone precursors [115]. Changes in gaseous and particulate levels in the major cities of southern China, Guangzhou (Figure 4.9(C)) and Shanghai (Figure 4.9(D)), resemble those of Wuhan during the city lockdown.

In contrast to southern and central China, PM_{2.5} in northern China during the outbreak period experienced remarkable increases (Figure 4.9(B)). During the three weeks of 2020-CLD, several severe haze events occurred in Beijing with the maximum daily PM_{2.5} level of $273.8 \mu\text{gm}^{-3}$. The CLD-mean surface PM_{2.5} in Beijing increased by $16.3 \mu\text{gm}^{-3}$ (+23.4%) and $30.6 \mu\text{gm}^{-3}$ (+55.1%) in comparison with CLIM-LNY and CLIM, respectively (Figure 4.9(B)). Nonetheless, NO₂ and SO₂ remained the lowest among the past six years, similar to that of the southern cities. Response of ozone concentration in Beijing followed a similar trend as that of PM_{2.5}, reaching a peak during the CLD. Daytime relationships between NO₂ and ozone concentrations in the winter of northern China show remarkable ozone titration during daytime, particularly with increasing PM_{2.5} which further attenuates the incoming solar radiation, but the titration effect becomes considerably alleviated during the city lockdown (Figure 4.10). Nationwide, 1515 state monitoring stations show clear hot spots of surface PM_{2.5} over northern China during the 2020-CLD (Figure 4.9(E)), although the national mean of the 2020-CLD PM_{2.5} was $52.1 \mu\text{gm}^{-3}$ which falls in the 1- σ range of variation of national climatology $54.7 \pm 6.1 \mu\text{gm}^{-3}$. Satellite-observed aerosol optical depth (AOD) based on the Moderate Resolution Imaging Spectroradiometer (MODIS) corroborates the persistent haze over northern China. Significantly high levels of AOD (> 0.8) were present over the North China Plain but did not occur in any previous year since 2015 (Figure 4.11), leading to 40-100% increases in AOD during the city lockdown.

Possible factors that explain enhanced PM_{2.5} and ozone levels in the face of declin-

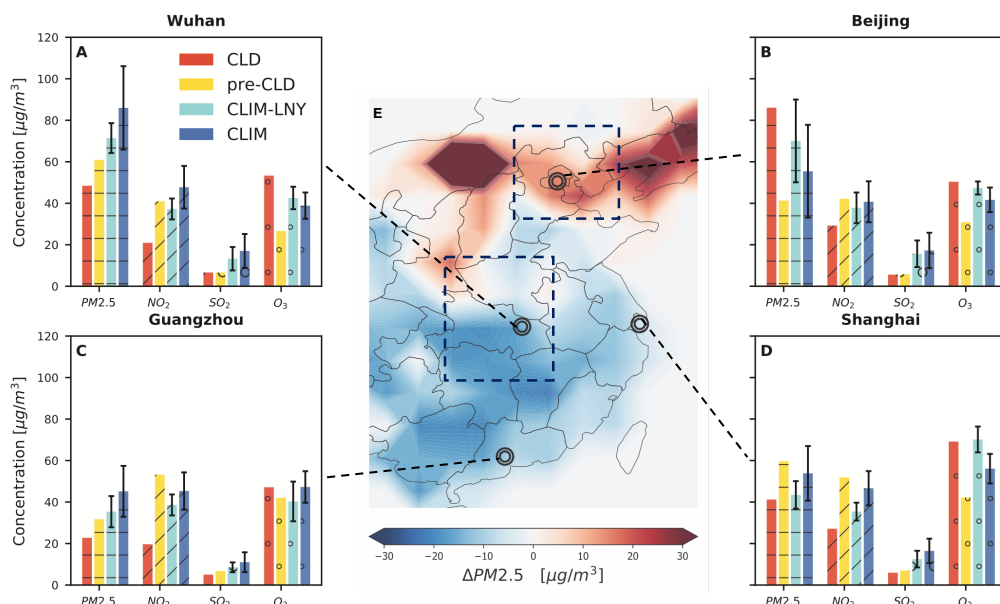


Figure 4.9: Ground-based station observation of particulate matter (aerodynamic diameter less than $2.5 \mu\text{m}$, $\text{PM}_{2.5}$), NO_2 , SO_2 , and ozone in eastern China including four megacities (A. Wuhan, B. Beijing, C. Guangzhou, and D. Shanghai). The figure compares the three-week averages during the city lockdown period (CLD), the three-week averages before the city lockdown (pre-CLD), the five-year climatology for 2015-2019 during the same period with CLD in the Chinese lunar calendar that covers the Lunar New Year (CLIM-LNY), and the five-year climatology for 2015-2019 during the same period with CLD in the Gregorian calendar (CLIM). Error bars indicate the standard deviations over multiple years. (E) The map of surface $\text{PM}_{2.5}$ changes in 2020-CLD compared to CLIM-LNY based on the 1515 state monitoring stations. The low-resolution patterns in the north and west are caused by the sparsity of stations. Two boxes indicate the Beijing-Tianjin-Hebei and central China regions. For ozone, $1 \mu\text{g}\text{m}^{-3}$ is approximately about 0.47 ppb under a standard condition.

ing precursor gas emissions include the complex chemistry of secondary aerosols and ozone [117, 142] as well as the meteorological influence [118]. Changes in relative humidity (RH), near-surface wind speed and direction, planetary boundary layer (PBL) height, and precipitation between the 2020-CLD and CLIM-LNY are shown in Figure 4.12, based on fifth-generation ECMWF global atmospheric reanalysis (ERA5). In northern China, which is climatologically dry during the wintertime, a larger than usual amount of moisture accumulated near the surface during the city lockdown, with a three-week mean RH of 55.2% and a maximum of 100%. Compared to the climatology, RH increased by 30-50% (Figure 4.12(A)), facilitating multiphase reactions for aerosol formation and growth [145]. Wind

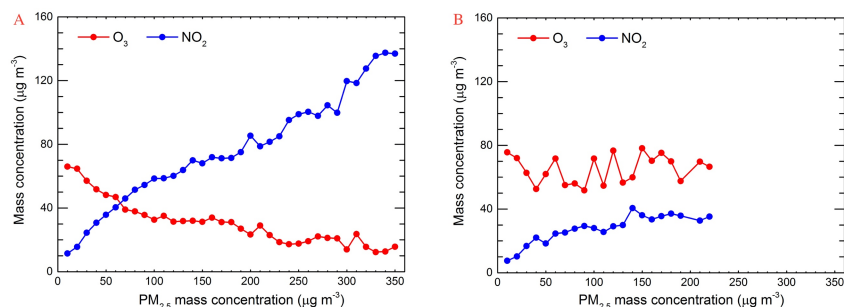


Figure 4.10: Daytime variation of ozone and NO₂ (10:00 to 16:00 LST) as a function of PM_{2.5} in the winter from 2015 to 2019 (A) and during 2020-CLD (B). During wintertime in north China, the weak insolation slows the atmospheric photochemistry processes. Therefore, very high NO_x emissions in the region cause remarkable ozone titration even during daytime, as shown in A, particularly with increasing PM_{2.5} which further attenuates the incoming solar radiation. However, during 2020-CLD, significant decrease in NO_x emissions alleviates the ozone titration, and during haze episodes, the ozone level is much higher than that during the winter from 2015 to 2019. The ozone concentration fluctuates at around $65 \mu\text{g m}^{-3}$ with PM_{2.5} exceeding $35 \mu\text{g m}^{-3}$, caused by complicated nonlinear ozone chemistry.

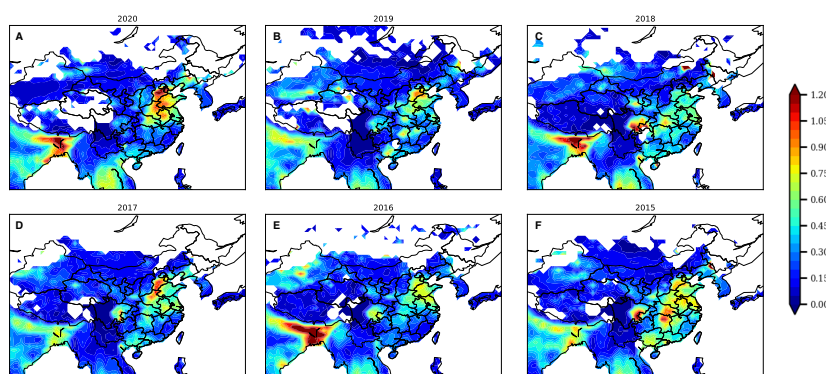


Figure 4.11: MODIS L3 AOD from Terra and Aqua during the same three-week period with 2020-CLD from 2015 to 2020.

conditions were also favorable for haze formation; in Beijing, the mean wind speed decreased by 20%, and winds switched to southerly that normally originate from the polluted industrial regions in Hebei Province (Figure 4.12(B)). Consistent with the increase in RH and the decrease in wind speed, PBL height in northern China generally declined during the city lockdown, inducing a stable boundary layer and stagnant air (Figure 4.12(C)). As a result, both ozone and PM_{2.5} increased in Beijing. During the same period, as precipitation occurred mainly over southern China, no significant wash-out occurred in northern China, conducive for haze development during the city lockdown. Also note that, as positive feedback to the meteorological variations [146], aerosols can reduce PBL height and stabilize lower atmosphere via their radiative effects [147], and suppress light precipitation via their microphysical effects [148].

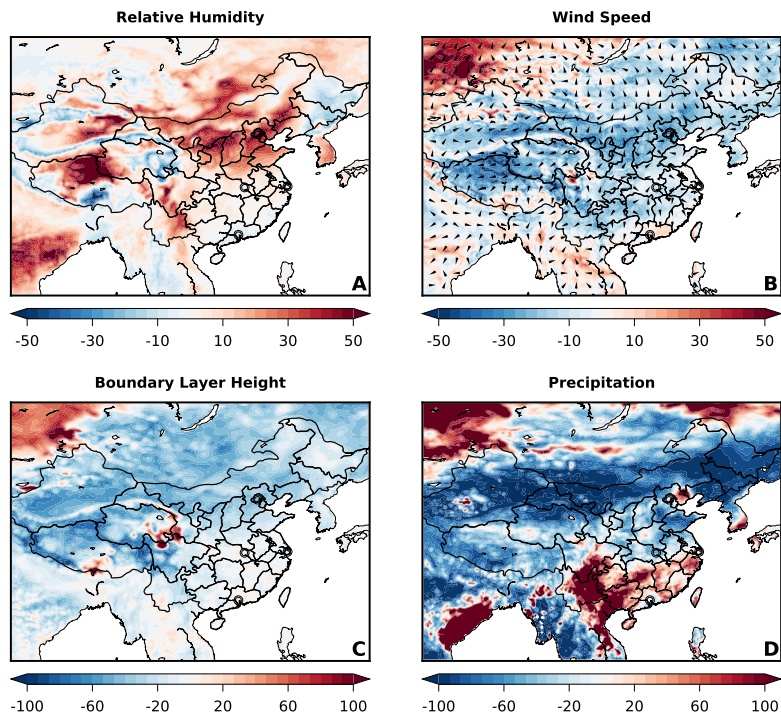


Figure 4.12: Fractional changes (%) in meteorological conditions between the 2020-CLD and the lunar new year climatology (CLIM-LNY) during 2015-2019 based on the ERA5 reanalysis data. (A) 1000-hPa relative humidity, (B) 10-meter wind speed (contours) and wind direction (vectors), (C) boundary-layer height, and (D) daily precipitation. Symbols in the maps indicate the location of the four major cities in Figure 4.9.

To reveal the physical and chemical mechanisms of the unexpected PM_{2.5} and ozone enhancement in northern China during the COVID19, we have conducted

atmospheric chemistry and transport simulations using the Weather Research and Forecast model online coupled with full gaseous and aerosol chemistry (WRF-Chem). The unusual particulate levels during the 2020 CLD in the Beijing-Tianjin-Hebei area (BTH) are well reproduced in our baseline simulations, in terms of consistent peak values about $200 \mu\text{g m}^{-3}$, well simulated temporal evolution over the three weeks, and small mean bias (MB) about $2.6 \mu\text{g m}^{-3}$ (Figure 4.13(A)). Surface ozone concentrations and diurnal cycles are comparable with ground-based observations (Figure 4.13(B)). Predicted aerosol chemical composition shows that organic aerosol (OA), nitrate, and sulfate are predominant species in BTH (Figure 4.14). When severe haze forms with a stable boundary layer and high humidity, inorganic fractions significantly increase with reduced OA, consistent with previous observations in the same area [149].

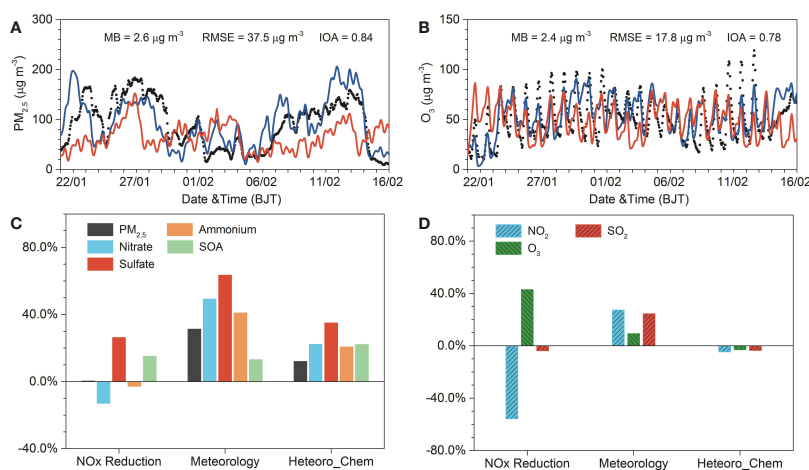


Figure 4.13: WRF-Chem simulated aerosol species and precursor gases during the COVID-19 city lockdown period in the Beijing-Tianjin-Hebei region, and their sensitivity to the altered emissions, meteorological conditions, and chemical pathways. (A) Time evolution of surface PM_{2.5} concentrations in the ground-based observations (black dots), the baseline simulation (blue line), and the sensitivity simulation with the climatological (2015-2019) meteorological conditions (red line, see details in Table 4.2). (B) The same with (A) but for ozone. (C) The simulated fractional changes in different aerosol species in response to changes in NO_x emissions, meteorological conditions, and the representation of heterogeneous chemistry. (D) The same with (C) but for gaseous pollutants including NO₂, SO₂, and O₃.

A series of model sensitivity simulations were conducted using altered emission rates, different meteorological conditions, and different sophistication of chemical schemes. An 80% NO_x emission reduction from all sectors in the model, consistent with the observed NO₂ reduction during the city-lockdown period, induces a 13.0%

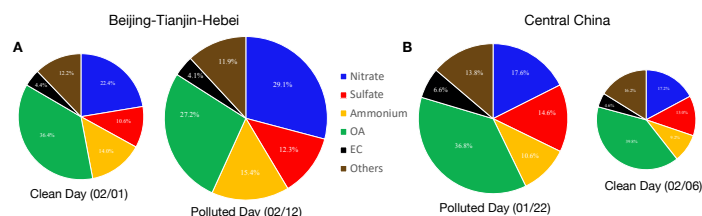


Figure 4.14: WRF-Chem simulated surface aerosol species over two characteristic regions: Beijing-Tianjin-Hebei in northern China and Central China. OA and EC are short for organic aerosol and elementary carbon, respectively.

reduction in nitrate aerosol but 26.3% and 15.1% increases in sulfate and secondary organic aerosol (SOA), respectively (Figure 4.13(C)). The latter increases can be attributed to the enhanced atmospheric oxidizing capacity following the 42.9% ozone increase (Figure 4.13(D)). Interestingly, the net PM_{2.5} change by NO_x reduction is not evident because of the cancellation of changes in different aerosol components. The meteorological influence on PM_{2.5} and ozone is assessed by comparing a pair of simulations with the meteorological conditions from this year and a multi-year climatology during the same period. It shows that due to the adverse ventilation conditions and anomalously high humidity during the city-lockdown period, all aerosol species are increased, with the largest fractional change of 63.5% for sulfate (Figure 4.13(D)). Total PM_{2.5} is increased by 31.3% accordingly. Moreover, heterogeneous chemistry processes contribute positively to the aerosol formation and haze development during the city-lockdown period, due to the concurrent high humidity and aerosol water. Our model assessment shows a 12.0% increase in PM_{2.5} contributed from heterogeneous chemistry in northern China. Comparisons among the simulations altering emissions, chemistry, and meteorology reveal that the unprecedented NO_x reduction during the COVID 19 does not significantly reduce aerosol formation because of the non-linear ozone and aerosol chemistry. In addition, meteorological variations are crucial in the haze formation in northern China by trapping pollutants in the urban area and inducing more efficient aerosol formation from heterogeneous chemistry. Because high humidity and atmospheric stability were absent over central China, including Wuhan, a gradual decline of PM_{2.5} during the lockdown period can be seen in both ground-based observations and model simulations. An increasing trend of ozone can also be identified in the temporal evolution. Aerosol chemical compositions generally are maintained, with OA accounting for 36-40% of total aerosol mass, and sulfate-nitrate-ammonium for

another 40% (Figure 4.14).

4.3.4 Conclusion

The COVID-19 outbreak led to unprecedented anthropogenic emission reductions from traffic and manufacturing sectors and the consequent city lockdowns. Hence, it offered a unique opportunity to assess the interplay between emissions, chemistry, and meteorology. Our synergistic analyses of the spatio-temporal distributions of PM and precursor gases, meteorological fields, and simulated PM formation pathways reveal a surprising PM exacerbation due to the unfavorable meteorological conditions, invigorated heterogeneous chemistry, and enhanced secondary aerosol formation with the elevated ozone oxidation capacity by NO_x reduction. In particular, our work provides unambiguous evidence that reduction in aerosol precursor emissions was compromised by multi-phase chemistry promoted by increased humidity. The role of multi-phase chemistry in haze formation is presently uncertain, and the findings here call for future research in this area.

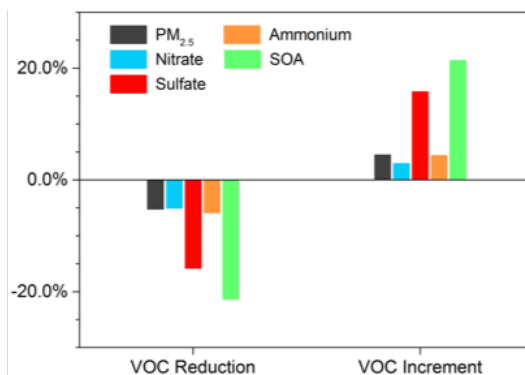


Figure 4.15: Simulated sensitivity of aerosol species and precursor gases to the VOC changes by 30%.

Reductions in NO_x and SO_2 from traffic and manufacturing sectors have long been considered as the normal protocol in implementing regulatory policies. Our work shows that such a protocol achieves only limited effects on PM and ozone levels, without simultaneous emission controls from power plants and heavy industry, such as petrochemical facilities. Therefore, we suggest a more comprehensive regulation of precursor gases from all possible sectors when developing an emission control strategy. For example, our model sensitivity experiments show 20% reduction in ozone and 5% reduction in $\text{PM}_{2.5}$ by implementing 30% reductions of VOCs from all possible emission sources (Figure 4.15). As opposed to the previous “Olympic Blue” and “APEC Blue” shutdowns, an unexpected increase in PM levels

in northern China occurred in a three-week period during the COVID-19 pandemic. The decisive role of meteorology in this unexpected haze formation in northern China during this episode underscores the importance of taking meteorological factors into account when short-term stringent emission controls are planned.

As the COVID-19 pandemic is still ongoing, the unexpected PM elevation has potentially profound implications for the airborne transmission of virus. A new emerging study shows plausible virus transmission via aerosols in populous areas [150]. Meanwhile, an exposure to high levels of PM can cause adverse effects on the respiratory and cardiovascular systems and possibly increase the fatality rate of COVID-19 [151]. Therefore, future work is urgently needed to establish the causal relationship between aerosol pollution and COVID-19.

BIBLIOGRAPHY

- [1] Arthur Schuster. “Radiation through a foggy atmosphere”. In: *The astrophysical journal* 21 (1905), p. 1.
- [2] Karl Schwarzschild. “On the equilibrium of the sun’s atmosphere”. In: *Nachrichten von der Königlich Gesellschaft der Wissenschaften zu Göttingen. Math.-phys. Klasse* 195 (1906), pp. 41–53.
- [3] Karl Schwarzschild. “Diffusion and absorption in the sun’s atmosphere”. In: *Sitzungsberichte der Königlich Preussischen Akademie der Wissenschaften Berlin* (1914), pp. 1183–1200.
- [4] AS Eddington. “On the radiative equilibrium of the stars”. In: *Monthly Notices of the Royal Astronomical Society* 77 (1916), pp. 16–35.
- [5] Subrahmanyan Chandrasekhar. “Radiative transfer.” In: *Oxford* (1950).
- [6] Y Fouquart. “Radiative transfer in climate models”. In: *Physically-Based Modelling and Simulation of Climate and Climatic Change* (1988), pp. 223–283.
- [7] Kuo-Nan Liou. *An introduction to atmospheric radiation*. Elsevier, 2002.
- [8] JT Kiehl and Kevin E Trenberth. “Earth’s annual global mean energy budget”. In: *Bulletin of the American meteorological society* 78.2 (1997), pp. 197–208.
- [9] Kevin E Trenberth, John T Fasullo, and Jeffrey Kiehl. “Earth’s global energy budget”. In: *Bulletin of the American Meteorological Society* 90.3 (2009), pp. 311–324.
- [10] Vijay Natraj et al. “Application of principal component analysis to high spectral resolution radiative transfer: A case study of the O₂ A band”. In: *Journal of Quantitative Spectroscopy and Radiative Transfer* 95.4 (2005), pp. 539–556.
- [11] Vijay Natraj, Run-Lie Shia, and Yuk L Yung. “On the use of principal component analysis to speed up radiative transfer calculations”. In: *Journal of Quantitative Spectroscopy and Radiative Transfer* 111.5 (2010), pp. 810–816.
- [12] Robert Spurr et al. “Linearization of the Principal Component Analysis method for radiative transfer acceleration: Application to retrieval algorithms and sensitivity studies”. In: *Journal of Quantitative Spectroscopy and Radiative Transfer* 125 (2013), pp. 1–17.
- [13] Pushkar Kopparla et al. “A fast and accurate PCA based radiative transfer model: Extension to the broadband shortwave region”. In: *Journal of Quantitative Spectroscopy and Radiative Transfer* 173 (2016), pp. 65–71.

- [14] Robert Spurr et al. “The application of principal component analysis (pca) to performance enhancement of hyperspectral radiative transfer computations”. In: *PRINCIPAL COMPONENT ANALYSIS* (2016), p. 33.
- [15] Graeme L Stephens and Andrew Heidinger. “Molecular line absorption in a scattering atmosphere. Part I: Theory”. In: *Journal of the atmospheric sciences* 57.10 (2000), pp. 1599–1614.
- [16] Xu Liu et al. “Development of a fast and accurate PCRTM radiative transfer model in the solar spectral region”. In: *Applied optics* 55.29 (2016), pp. 8236–8247.
- [17] NJ King and G Vaughan. “Using passive remote sensing to retrieve the vertical variation of cloud droplet size in marine stratocumulus: An assessment of information content and the potential for improved retrievals from hyperspectral measurements”. In: *Journal of Geophysical Research: Atmospheres* 117.D15 (2012).
- [18] Yufei Ai et al. “Deep convective cloud characterizations from both broadband imager and hyperspectral infrared sounder measurements”. In: *Journal of Geophysical Research: Atmospheres* 122.3 (2017), pp. 1700–1712.
- [19] Hartmut H Aumann et al. “AIRS/AMSU/HSB on the Aqua mission: Design, science objectives, data products, and processing systems”. In: *IEEE Transactions on Geoscience and Remote Sensing* 41.2 (2003), pp. 253–264.
- [20] Richard J Kohrman and Scott D Luce. “Mechanical design of the crosstrack infrared sounder (CrIS)”. In: *Infrared Spaceborne Remote Sensing IX*. Vol. 4486. International Society for Optics and Photonics. 2002, pp. 445–455.
- [21] Yong Han et al. “Suomi NPP CrIS measurements, sensor data record algorithm, calibration and validation activities, and record data quality”. In: *Journal of Geophysical Research: Atmospheres* 118.22 (2013), pp. 12–734.
- [22] Fiona Hilton et al. “Hyperspectral Earth observation from IASI: Five years of accomplishments”. In: *bulletin of the american meteorological Society* 93.3 (2012), pp. 347–370.
- [23] Jun Yang et al. “Introducing the new generation of Chinese geostationary weather satellites, Fengyun-4”. In: *Bulletin of the American Meteorological Society* 98.8 (2017), pp. 1637–1658.
- [24] Pieternel F Levelt et al. “The ozone monitoring instrument”. In: *IEEE Transactions on geoscience and remote sensing* 44.5 (2006), pp. 1093–1101.
- [25] JP Veefkind et al. “TROPOMI on the ESA Sentinel-5 Precursor: A GMES mission for global observations of the atmospheric composition for climate, air quality and ozone layer applications”. In: *Remote sensing of environment* 120 (2012), pp. 70–83.

- [26] L Flynn et al. “Performance of the ozone mapping and profiler suite (OMPS) products”. In: *Journal of Geophysical Research: Atmospheres* 119.10 (2014), pp. 6181–6195.
- [27] J Callies et al. “GOME-2-Metop’s second-generation sensor for operational ozone monitoring”. In: *ESA bulletin* 102 (2000), pp. 28–36.
- [28] David Crisp et al. “The on-orbit performance of the Orbiting Carbon Observatory-2 (OCO-2) instrument and its radiometrically calibrated products”. In: *Atmospheric Measurement Techniques* 10.1 (2017), pp. 59–81.
- [29] Yi Liu et al. “Optimization of the instrument configuration for TanSat CO₂ spectrometer”. In: *Chinese Science Bulletin* 58.27 (2013), pp. 2787–2789.
- [30] Debra Wunch et al. “The total carbon column observing network”. In: *Philosophical Transactions of the Royal Society A: Mathematical, Physical and Engineering Sciences* 369.1943 (2011), pp. 2087–2112.
- [31] D Fu et al. “Near-infrared remote sensing of Los Angeles trace gas distributions from a mountaintop site”. In: *Atmospheric Measurement Techniques* 7.3 (2014), pp. 713–729.
- [32] Zhao-Cheng Zeng et al. “Constraining aerosol vertical profile in the boundary layer using hyperspectral measurements of oxygen absorption”. In: *Geophysical Research Letters* 45.19 (2018), pp. 10–772.
- [33] Minzheng Duan, Qilong Min, and Jiangnan Li. “A fast radiative transfer model for simulating high-resolution absorption bands”. In: *Journal of Geophysical Research: Atmospheres* 110.D15 (2005).
- [34] Z. Zhang et al. “A fast infrared radiative transfer model based on the adding–doubling method for hyperspectral remote-sensing applications”. In: *Journal of Quantitative Spectroscopy and Radiative Transfer* 105.2 (2007), pp. 243–263.
- [35] C. Wang, P. Yang, and X. Liu. “A high-spectral-resolution radiative transfer model for simulating multilayered clouds and aerosols in the infrared spectral region”. In: *Journal of Atmospheric Sciences* 72.2 (2015), pp. 926–942.
- [36] Pushkar Kopparla et al. “PCA-based radiative transfer: Improvements to aerosol scheme, vertical layering and spectral binning”. In: *Journal of Quantitative Spectroscopy and Radiative Transfer* 198 (2017), pp. 104–111.
- [37] P Somkuti et al. “Application of a PCA-based fast Radiative transfer model to XCO₂ retrievals in the shortwave infrared”. In: *Journal of Geophysical Research: Atmospheres* 122.19 (2017), pp. 10–477.
- [38] Xu Liu et al. “Principal component-based radiative transfer model for hyperspectral sensors: Theoretical concept”. In: *Applied Optics* 45.1 (2006), pp. 201–209.

- [39] Jean-Luc Moncet et al. “Infrared radiance modeling by optimal spectral sampling”. In: *Journal of the atmospheric sciences* 65.12 (2008), pp. 3917–3934.
- [40] László Monostori. “AI and machine learning techniques for managing complexity, changes and uncertainties in manufacturing”. In: *Engineering applications of artificial intelligence* 16.4 (2003), pp. 277–291.
- [41] Michael I Jordan and Tom M Mitchell. “Machine learning: Trends, perspectives, and prospects”. In: *Science* 349.6245 (2015), pp. 255–260.
- [42] Mahdieh Poostchi et al. “Image analysis and machine learning for detecting malaria”. In: *Translational Research* 194 (2018), pp. 36–55.
- [43] Céline Cornet et al. “Case study of inhomogeneous cloud parameter retrieval from MODIS data”. In: *Geophysical research letters* 32.13 (2005).
- [44] R Martin et al. “Machine learning techniques for daily solar energy prediction and interpolation using numerical weather models”. In: *Concurrency and Computation: Practice and Experience* 28.4 (2016), pp. 1261–1274.
- [45] Atsu SS Dorvlo, Joseph A Jervase, and Ali Al-Lawati. “Solar radiation estimation using artificial neural networks”. In: *Applied Energy* 71.4 (2002), pp. 307–319.
- [46] Luis F Zarzalejo, Lourdes Ramirez, and Jesus Polo. “Artificial intelligence techniques applied to hourly global irradiance estimation from satellite-derived cloud index”. In: *Energy* 30.9 (2005), pp. 1685–1697.
- [47] Hideaki Takenaka et al. “Estimation of solar radiation using a neural network based on radiative transfer”. In: *Journal of Geophysical Research: Atmospheres* 116.D8 (2011).
- [48] M Taylor et al. “Neural network radiative transfer solvers for the generation of high resolution solar irradiance spectra parameterized by cloud and aerosol parameters”. In: *Journal of Quantitative Spectroscopy and Radiative Transfer* 168 (2016), pp. 176–192.
- [49] Chao Liu et al. “A spectral data compression (SDCOMP) radiative transfer model for high-spectral-resolution radiation simulations”. In: *Journal of the Atmospheric Sciences* 77.6 (2020), pp. 2055–2066.
- [50] George Cybenko. “Approximation by superpositions of a sigmoidal function”. In: *Mathematics of control, signals and systems* 2.4 (1989), pp. 303–314.
- [51] Kurt Hornik, Maxwell Stinchcombe, and Halbert White. “Multilayer feed-forward networks are universal approximators”. In: *Neural networks* 2.5 (1989), pp. 359–366.

- [52] Xavier Glorot, Antoine Bordes, and Yoshua Bengio. “Deep sparse rectifier neural networks”. In: *Proceedings of the fourteenth international conference on artificial intelligence and statistics*. JMLR Workshop and Conference Proceedings. 2011, pp. 315–323.
- [53] Reima Eresmaa and Anthony P McNally. “Diverse profile datasets based on the CAMS atmospheric composition forecasting system”. In: *ECMWF Rep* (2016).
- [54] Ian Goodfellow, Yoshua Bengio, and Aaron Courville. *Deep learning*. MIT press, 2016.
- [55] Diederik P Kingma and Jimmy Ba. “Adam: A method for stochastic optimization”. In: *arXiv preprint arXiv:1412.6980* (2014).
- [56] Sauro Succi and Peter V Coveney. “Big data: the end of the scientific method?” In: *Philosophical Transactions of the Royal Society A* 377.2142 (2019), p. 20180145.
- [57] RJD Spurr, TP Kurosu, and KV Chance. “A linearized discrete ordinate radiative transfer model for atmospheric remote-sensing retrieval”. In: *Journal of Quantitative Spectroscopy and Radiative Transfer* 68.6 (2001), pp. 689–735.
- [58] Yong Chen et al. “Validation of the community radiative transfer model by using CloudSat data”. In: *Journal of Geophysical Research: Atmospheres* 113.D8 (2008).
- [59] R Saunders, M Matricardi, and P Brunel. “An improved fast radiative transfer model for assimilation of satellite radiance observations”. In: *Quarterly Journal of the Royal Meteorological Society* 125.556 (1999), pp. 1407–1425.
- [60] Fuzhong Weng et al. “Advanced Radiative Transfer Modeling System (ARMS): A new-generation satellite observation operator developed for numerical weather prediction and remote sensing applications”. In: *Adv. Atmos. Sci.* 37.2 (2020), pp. 131–136.
- [61] Sandrine Bony et al. “Thermodynamic control of anvil cloud amount”. In: *Proceedings of the National Academy of Sciences* 113.32 (2016), pp. 8927–8932.
- [62] Dennis L Hartmann and Kristin Larson. “An important constraint on tropical cloud-climate feedback”. In: *Geophysical research letters* 29.20 (2002), pp. 12–1.
- [63] Richard S Lindzen, Ming-Dah Chou, and Arthur Y Hou. “Does the earth have an adaptive infrared iris?” In: *Bulletin of the American Meteorological Society* 82.3 (2001), pp. 417–432.

- [64] Hui Su et al. “Tightening of tropical ascent and high clouds key to precipitation change in a warmer climate”. In: *Nature communications* 8.1 (2017), pp. 1–9.
- [65] AD Collard and AP McNally. “The assimilation of infrared atmospheric sounding interferometer radiances at ECMWF”. In: *Quarterly Journal of the Royal Meteorological Society: A journal of the atmospheric sciences, applied meteorology and physical oceanography* 135.641 (2009), pp. 1044–1058.
- [66] AP McNally. “The direct assimilation of cloud-affected satellite infrared radiances in the ECMWF 4D-Var”. In: *Quarterly Journal of the Royal Meteorological Society: A journal of the atmospheric sciences, applied meteorology and physical oceanography* 135.642 (2009), pp. 1214–1229.
- [67] EG Pavelin, SJ English, and JR Eyre. “The assimilation of cloud-affected infrared satellite radiances for numerical weather prediction”. In: *Quarterly Journal of the Royal Meteorological Society: A journal of the atmospheric sciences, applied meteorology and physical oceanography* 134.632 (2008), pp. 737–749.
- [68] Alan J Geer, Peter Bauer, and Christopher W O’Dell. “A revised cloud overlap scheme for fast microwave radiative transfer in rain and cloud”. In: *Journal of applied meteorology and climatology* 48.11 (2009), pp. 2257–2270.
- [69] Lin Tian and Judith A Curry. “Cloud overlap statistics”. In: *Journal of Geophysical Research: Atmospheres* 94.D7 (1989), pp. 9925–9935.
- [70] Xiuhong Chen, Xianglei Huang, and Xu Liu. “Non-negligible effects of cloud vertical overlapping assumptions on longwave spectral fingerprinting studies”. In: *Journal of Geophysical Research: Atmospheres* 118.13 (2013), pp. 7309–7320.
- [71] Alan J Geer et al. “All-sky satellite data assimilation at operational weather forecasting centres”. In: *Quarterly Journal of the Royal Meteorological Society* 144.713 (2018), pp. 1191–1217.
- [72] Alan J Geer, Stefano Migliorini, and Marco Matricardi. “All-sky assimilation of infrared radiances sensitive to mid-and upper-tropospheric moisture and cloud”. In: *Atmospheric Measurement Techniques* 12.9 (2019), pp. 4903–4929.
- [73] Hartmut H Aumann et al. “Evaluation of radiative transfer models with clouds”. In: *Journal of Geophysical Research: Atmospheres* 123.11 (2018), pp. 6142–6157.
- [74] ECMWF ECMWF. *IFS documentation CY33r1*. Tech. rep. part IV, Tech. rep., ECMWF, available at: <http://www.ecmwf.int/research> . . . , 2009.

- [75] Yong Han. “JCSDA community radiative transfer model (CRTM): Version 1”. In: (2006).
- [76] L Garand et al. “Radiance and Jacobian intercomparison of radiative transfer models applied to HIRS and AMSU channels”. In: *Journal of Geophysical Research: Atmospheres* 106.D20 (2001), pp. 24017–24031.
- [77] Fuzhong Weng and Quanhua Liu. “Satellite data assimilation in numerical weather prediction models. Part I: Forward radiative transfer and Jacobian modeling in cloudy atmospheres”. In: *Journal of Atmospheric Sciences* 60.21 (2003), pp. 2633–2646.
- [78] Jun Li et al. “Satellite All-sky Infrared Radiance Assimilation: Recent Progress and Future Perspectives”. In: *Advances in Atmospheric Sciences* (2021), pp. 1–13.
- [79] Bryan A Baum et al. “Bulk scattering properties for the remote sensing of ice clouds. Part I: Microphysical data and models”. In: *Journal of Applied Meteorology* 44.12 (2005), pp. 1885–1895.
- [80] KN Bower et al. “A parameterization of warm clouds for use in atmospheric general circulation models”. In: *Journal of Atmospheric Sciences* 51.19 (1994), pp. 2722–2732.
- [81] SC Ou et al. “Remote sounding of cirrus cloud optical depths and ice crystal sizes from AVHRR data: Verification using FIRE II IFO measurements”. In: *Journal of Atmospheric Sciences* 52.23 (1995), pp. 4143–4158.
- [82] Steve SC Ou et al. “Retrieval of cirrus cloud properties from the atmospheric infrared sounder: the k-coefficient approach using cloud-cleared radiances as input”. In: *IEEE Transactions on Geoscience and Remote Sensing* 51.2 (2012), pp. 1010–1024.
- [83] P van Delst, EH Liu, and L Bi. “Cloud fraction in the CRTM”. In: *JCSDA Office Note CRTM-4, Rrev 71147* (2016), p. 36.
- [84] Martin Arjovsky, Soumith Chintala, and Léon Bottou. “Wasserstein generative adversarial networks”. In: *International conference on machine learning*. PMLR. 2017, pp. 214–223.
- [85] Yossi Rubner, Carlo Tomasi, and Leonidas J Guibas. “The earth mover’s distance as a metric for image retrieval”. In: *International journal of computer vision* 40.2 (2000), pp. 99–121.
- [86] Elizabeth A Barnes et al. “Exploring recent trends in Northern Hemisphere blocking”. In: *Geophysical Research Letters* 41.2 (2014), pp. 638–644.
- [87] Lantao Sun, Judith Perlwitz, and Martin Hoerling. “What caused the recent “Warm Arctic, Cold Continents” trend pattern in winter temperatures?” In: *Geophysical Research Letters* 43.10 (2016), pp. 5345–5352.

- [88] Judah Cohen, Karl Pfeiffer, and Jennifer A Francis. “Warm Arctic episodes linked with increased frequency of extreme winter weather in the United States”. In: *Nature communications* 9.1 (2018), pp. 1–12.
- [89] Adam A Scaife et al. “European climate extremes and the North Atlantic Oscillation”. In: *Journal of Climate* 21.1 (2008), pp. 72–83.
- [90] Judah Cohen et al. “Recent Arctic amplification and extreme mid-latitude weather”. In: *Nature geoscience* 7.9 (2014), pp. 627–637.
- [91] Jennifer A Francis and Stephen J Vavrus. “Evidence for a wavier jet stream in response to rapid Arctic warming”. In: *Environmental Research Letters* 10.1 (2015), p. 014005.
- [92] Tapio Schneider, Tobias Bischoff, and Hanna Plotka. “Physics of changes in synoptic midlatitude temperature variability”. In: *Journal of Climate* 28.6 (2015), pp. 2312–2331.
- [93] DJ Seidel et al. *Widening of the tropical belt in a changing climate*. *Nat Geosci.* 2008.
- [94] J Screen, I Simmonds, and J Francis. “Coauthors, 2018: Elucidating the effects of arctic sea ice loss on Northern Hemisphere climate”. In: *Nat. Geosci* 11 (), pp. 155–163.
- [95] B Booth and NJ Dunstone. “Halloran PRet al”. In: *Aerosols implicated as a prime driver of twentieth-century North Atlantic climate variability*. *Nature* 484 (2012), pp. 228–32.
- [96] Jiwen Fan et al. “Review of aerosol–cloud interactions: Mechanisms, significance, and challenges”. In: *Journal of the Atmospheric Sciences* 73.11 (2016), pp. 4221–4252.
- [97] John H Seinfeld et al. “Improving our fundamental understanding of the role of aerosol- cloud interactions in the climate system”. In: *Proceedings of the National Academy of Sciences* 113.21 (2016), pp. 5781–5790.
- [98] Yuan Wang, Jonathan H Jiang, and Hui Su. “Atmospheric responses to the redistribution of anthropogenic aerosols”. In: *Journal of Geophysical Research: Atmospheres* 120.18 (2015), pp. 9625–9641.
- [99] Yuan Wang et al. “Elucidating the role of anthropogenic aerosols in Arctic sea ice variations”. In: *Journal of Climate* 31.1 (2018), pp. 99–114.
- [100] Gang Chen et al. “Local finite-amplitude wave activity as an objective diagnostic of midlatitude extreme weather”. In: *Geophysical Research Letters* 42.24 (2015), pp. 10–952.
- [101] Julien Cattiaux et al. “Sinuosity of midlatitude atmospheric flow in a warming world”. In: *Geophysical Research Letters* 43.15 (2016), pp. 8259–8268.

- [102] Chaim I Garfinkel and Darryn W Waugh. “Tropospheric Rossby wave breaking and variability of the latitude of the eddy-driven jet”. In: *Journal of Climate* 27.18 (2014), pp. 7069–7085.
- [103] Yayoi Harada et al. “The JRA-55 Reanalysis: Representation of atmospheric circulation and climate variability”. In: *Journal of the Meteorological Society of Japan. Ser. II* 94.3 (2016), pp. 269–302.
- [104] Johann Feichter et al. “Nonlinear aspects of the climate response to greenhouse gas and aerosol forcing”. In: *Journal of climate* 17.12 (2004), pp. 2384–2398.
- [105] Yi Ming and V Ramaswamy. “Nonlinear climate and hydrological responses to aerosol effects”. In: *Journal of Climate* 22.6 (2009), pp. 1329–1339.
- [106] Yi Ming and V Ramaswamy. “A model investigation of aerosol-induced changes in tropical circulation”. In: *Journal of climate* 24.19 (2011), pp. 5125–5133.
- [107] Dim Coumou, Jascha Lehmann, and Johanna Beckmann. “The weakening summer circulation in the Northern Hemisphere mid-latitudes”. In: *Science* 348.6232 (2015), pp. 324–327.
- [108] Andrew Rhines et al. “Seasonally resolved distributional trends of North American temperatures show contraction of winter variability”. In: *Journal of Climate* 30.3 (2017), pp. 1139–1157.
- [109] Michael E Mann et al. “Projected changes in persistent extreme summer weather events: The role of quasi-resonant amplification”. In: *Science advances* 4.10 (2018), eaat3272.
- [110] James A Screen and Ian Simmonds. “Exploring links between Arctic amplification and mid-latitude weather”. In: *Geophysical Research Letters* 40.5 (2013), pp. 959–964.
- [111] Zhisheng An et al. “Severe haze in northern China: A synergy of anthropogenic emissions and atmospheric processes”. In: *Proceedings of the National Academy of Sciences* 116.18 (2019), pp. 8657–8666.
- [112] Bin Zhao et al. “Change in household fuels dominates the decrease in PM_{2.5} exposure and premature mortality in China in 2005–2015”. In: *Proceedings of the National Academy of Sciences* 115.49 (2018), pp. 12401–12406.
- [113] Qiang Zhang et al. “Drivers of improved PM_{2.5} air quality in China from 2013 to 2017”. In: *Proceedings of the National Academy of Sciences* 116.49 (2019), pp. 24463–24469.
- [114] Guohui Li et al. “Widespread and persistent ozone pollution in eastern China during the non-winter season of 2015: observations and source attributions”. In: *Atmospheric Chemistry and Physics* 17.4 (2017), pp. 2759–2774.

- [115] Ke Li et al. “Anthropogenic drivers of 2013–2017 trends in summer surface ozone in China”. In: *Proceedings of the National Academy of Sciences* 116.2 (2019), pp. 422–427.
- [116] Gehui Wang et al. “Persistent sulfate formation from London Fog to Chinese haze”. In: *Proceedings of the National Academy of Sciences* 113.48 (2016), pp. 13630–13635.
- [117] Fang Zhang et al. “An unexpected catalyst dominates formation and radiative forcing of regional haze”. In: *Proceedings of the National Academy of Sciences* 117.8 (2020), pp. 3960–3966.
- [118] Lu Mao et al. “An observation-based perspective of winter haze days in four major polluted regions of China”. In: *National Science Review* 6.3 (2019), pp. 515–523.
- [119] Shuxiao Wang et al. “Quantifying the air pollutants emission reduction during the 2008 Olympic Games in Beijing”. In: *Environmental science & technology* 44.7 (2010), pp. 2490–2496.
- [120] Kan Huang, Xingying Zhang, and Yanfen Lin. “The “APEC Blue” phenomenon: Regional emission control effects observed from space”. In: *Atmospheric Research* 164 (2015), pp. 65–75.
- [121] Ran Meng et al. “Analysis of the 2014 “APEC blue” in Beijing using more than one decade of satellite observations: lessons learned from radical emission control measures”. In: *Remote Sensing* 7.11 (2015), pp. 15224–15243.
- [122] Georg A Grell et al. “Fully coupled “online” chemistry within the WRF model”. In: *Atmospheric Environment* 39.37 (2005), pp. 6957–6975.
- [123] Guohui Li et al. “Impacts of HONO sources on the photochemistry in Mexico City during the MCMA-2006/MILAGO Campaign”. In: *Atmospheric Chemistry and Physics* 10.14 (2010), pp. 6551–6567.
- [124] Guohui Li et al. “Aerosol effects on the photochemistry in Mexico City during MCMA-2006/MILAGRO campaign”. In: *Atmospheric Chemistry and Physics* 11.11 (2011), pp. 5169–5182.
- [125] Guohui Li et al. “Simulations of organic aerosol concentrations in Mexico City using the WRF-CHEM model during the MCMA-2006/MILAGRO campaign”. In: *Atmospheric Chemistry and Physics* 11.8 (2011), pp. 3789–3809.
- [126] G Li et al. “Contribution of garbage burning to chloride and PM 2.5 in Mexico City”. In: *Atmospheric Chemistry and Physics* 12.18 (2012), pp. 8751–8761.
- [127] KM Foley et al. “Incremental testing of the Community Multiscale Air Quality (CMAQ) modeling system version 4.7”. In: *Geoscientific Model Development* 3.1 (2010), pp. 205–226.

- [128] Athanasios Nenes, Spyros N Pandis, and Christodoulos Pilinis. “ISORROPIA: A new thermodynamic equilibrium model for multiphase multicomponent inorganic aerosols”. In: *Aquatic geochemistry* 4.1 (1998), pp. 123–152.
- [129] Qiang Zhang et al. “Asian emissions in 2006 for the NASA INTEX-B mission”. In: *Atmospheric Chemistry and Physics* 9.14 (2009), pp. 5131–5153.
- [130] Alex Guenther et al. “Estimates of global terrestrial isoprene emissions using MEGAN (Model of Emissions of Gases and Aerosols from Nature)”. In: *Atmospheric Chemistry and Physics* 6.11 (2006), pp. 3181–3210.
- [131] HS Halliday et al. “Using short-term CO/CO₂ ratios to assess air mass differences over the Korean Peninsula during KORUS-AQ”. In: *Journal of Geophysical Research: Atmospheres* 124.20 (2019), pp. 10951–10972.
- [132] Ru-Jin Huang et al. “High secondary aerosol contribution to particulate pollution during haze events in China”. In: *Nature* 514.7521 (2014), pp. 218–222.
- [133] David G Streets et al. “Emissions estimation from satellite retrievals: A review of current capability”. In: *Atmospheric Environment* 77 (2013), pp. 1011–1042.
- [134] Yang Wang et al. “Vertical profiles of NO₂, SO₂, HONO, HCHO, CHOCHO and aerosols derived from MAX-DOAS measurements at a rural site in the central western North China Plain and their relation to emission sources and effects of regional transport”. In: *Atmospheric Chemistry and Physics* 19.8 (2019), pp. 5417–5449.
- [135] Song-You Hong and Jeong-Ock Jade Lim. “The WRF single-moment 6-class microphysics scheme (WSM6)”. In: *Asia-Pacific Journal of Atmospheric Sciences* 42.2 (2006), pp. 129–151.
- [136] Zaviša I Janić. *Nonsingular implementation of the Mellor-Yamada level 2.5 scheme in the NCEP Meso model*. US Department of Commerce, National Oceanic and Atmospheric Administration . . . , 2001.
- [137] Fei Chen and Jimy Dudhia. “Coupling an advanced land surface–hydrology model with the Penn State–NCAR MM5 modeling system. Part I: Model implementation and sensitivity”. In: *Monthly weather review* 129.4 (2001), pp. 569–585.
- [138] Ming-Dah Chou et al. “A thermal infrared radiation parameterization for atmospheric studies”. In: (2001).
- [139] Ming-Dah Chou and Max J Suarez. “A Solar Radiation Parameterization for Atmospheric Studies. Volume 15”. In: (1999).

- [140] Larry W Horowitz et al. “A global simulation of tropospheric ozone and related tracers: Description and evaluation of MOZART, version 2”. In: *Journal of geophysical research: Atmospheres* 108.D24 (2003).
- [141] Dao-Yi Gong et al. “Observed holiday aerosol reduction and temperature cooling over East Asia”. In: *Journal of Geophysical Research: Atmospheres* 119.11 (2014), pp. 6306–6324.
- [142] Jeffrey I Steinfeld. “Atmospheric chemistry and physics: from air pollution to climate change”. In: *Environment: Science and Policy for Sustainable Development* 40.7 (1998), pp. 26–26.
- [143] Misti Levy et al. “Measurements of nitrous acid (HONO) using ion drift-chemical ionization mass spectrometry during the 2009 SHARP field campaign”. In: *Atmospheric environment* 94 (2014), pp. 231–240.
- [144] Jiarui Wu et al. “Aerosol–photolysis interaction reduces particulate matter during wintertime haze events”. In: *Proceedings of the National Academy of Sciences* 117.18 (2020), pp. 9755–9761.
- [145] Xuexi Tie et al. “Severe pollution in China amplified by atmospheric moisture”. In: *Scientific Reports* 7.1 (2017), pp. 1–8.
- [146] Zhanqing Li et al. “East Asian study of tropospheric aerosols and their impact on regional clouds, precipitation, and climate (EAST-AIRCPC)”. In: *Journal of Geophysical Research: Atmospheres* 124.23 (2019), pp. 13026–13054.
- [147] Yuan Wang et al. “New Directions: Light absorbing aerosols and their atmospheric impacts”. In: *Atmospheric Environment* 81 (2013), pp. 713–715.
- [148] Yuan Wang et al. “Toward reconciling the influence of atmospheric aerosols and greenhouse gases on light precipitation changes in Eastern China”. In: *Journal of Geophysical Research: Atmospheres* 121.10 (2016), pp. 5878–5887.
- [149] Song Guo et al. “Remarkable nucleation and growth of ultrafine particles from vehicular exhaust”. In: *Proceedings of the National Academy of Sciences* 117.7 (2020), pp. 3427–3432.
- [150] Yuan Liu et al. “Aerodynamic analysis of SARS-CoV-2 in two Wuhan hospitals”. In: *Nature* 582.7813 (2020), pp. 557–560.
- [151] Xiao Wu et al. “Exposure to air pollution and COVID-19 mortality in the United States”. In: *MedRxiv* (2020).